GBT MEMO 129

Modeling and Analysis of the Green Bank Telescope Control System

Prepared by:
Wodek Gawronski and Ben Parvin

Pasadena
April 29, 1995

Abstract

The servo system of the Green Bank Telescope is modeled and analyzed. The model includes the finite element structural model (in modal coordinates), gearboxes and drives, PI and feedforward controllers, and wind disturbance models. Based on the developed model the antenna closed-loop performance was analyzed.

The analysis includes:
1. Checking the properties of the structure (illustrated with its transfer functions),
2. Reduction of the structure model,
3. Simulations of the closed-loop (PI) system performance (step responses), transfer functions, checking cross-coupling effects,
4. Analysis of the wind disturbances and simulations of the antenna pointing errors due to steady winds and wind gusts,
5. Analysis of the feedforward controller performance, its transfer functions and cross-coupling effects, as well as the simulations of the tracking errors for tracking trajectories with rates close to the maximum allowable,
6. Implementation and performance analysis of the PCD command preprocessor, to reduce errors and overshoots while slewing and tracking commands that exceed rate and acceleration limits,
7. Checking the antenna performance in wind, with implemented rate and acceleration limits,
8. Analysis of the antenna performance with the dry friction and stiction for low rate motion,
9. Evaluation of the accuracy of the antenna model and simulations.

The analysis shows that:

1. The structural dynamics do not display any abnormal modes that should be of concern. The lowest simulated closed-loop structural resonance is at 0.68 Hz. This is above GBT Design Specification which is 0.5 Hz or better,
2. The axes control loops as designed by RSi/PCD perform to the requirement of the GBT specification,
3. The simulated settling time for a one degree step is about 12 seconds for elevation, and 15 seconds for cross-elevation,
4. The command preprocessor, with the rate and the acceleration limits levels structural excitation and overshoot. The calculated overshoot was below 10 mdeg for large steps (1 deg or more),
5. The worst case pointing performance of the GBT is for wind gusting along the elevation axis. The simulations for this wind direction at a speed of 7 m/s (steady state and gusting) indicate an rms pointing error of 13.3 arcsecond in cross-elevation, and less than 1 arcsec in elevation. The GBT Design Specification is 14 arcsec, thus the requirement is met,
6. The dry friction and stiction does not have significant impact on the antenna dynamics. Limit cycling amplitude is below 1 mdeg, and it does not improve the damping of the flexible oscillations.

Contents:

1. Introduction

The control system model of the Green Bank telescope was developed in three stages. First, the structural model was obtained from the finite element model. Second, the rate-loop model was developed by adding two elevation and four azimuth drives, including gearboxes and motors to the structural model. Third, the position loop model was obtained by closing the feedback loop in azimuth and elevation around the rate-loop model.

The antenna position-loop performance was evaluated by the simulations of the antenna responses to the step commands both in azimuth and elevation, to the wind disturbances (steady, and gusts), and by analysis of the closed-loop transfer functions.

The antenna control system was upgraded by adding the feedforward gain. This upgrade increases servo bandwidth, while the wind disturbance rejection properties remain unchanged. The feedforward servo performance is illustrated with its transfer function (which shows the increased bandwidth) and with the tracking of trajectories at rates close to the rate limits of the antenna (0.67 deg/sec in azimuth, and 0.33 deg/sec in elevation).

Next, the non-linear simulations of the antenna control system are presented. The rate and acceleration limits are imposed for the azimuth and elevation motion. If the limits are exceeded (i.e. by imposing step command), a non-linear antenna response is observed, which may lead to unwelcome limit cycling. To avoid this, the command pre-processor as developed by PCD, is applied. The antenna dynamics with the pre-processor is simulated. Also, the rolling friction and stiction may affect the system dynamics, especially for low-rate motions. This phenomenon was simulated for slow rolling in azimuth, e.g. at final stages of the step response.

Finally, based on the previous experiences with the DSN antennas, the accuracy of the modeling and simulations was discussed.

2. Structural Model

The GBT finite element model was developed using the IDEAS software. The antenna structure was symmetric with respect to its Y-Z plane, therefore it was possible to develop the finite element model of the symmetric half of the structure without loosing information about the other half. This approach was necessary since the finite element model consisted of the large number of elements, see Ref.[1], and the available computer had limited memory capacity.

For the control design purposes the structural model was developed in modal coordinates. In this way, the dimension of the model was much smaller, than the model in physical coordinates. The size of the modal model is twice the number of modes, while the size of a model in the physical coordinates is twice the number of the nodal degrees of freedom. The finite element model consisted of 18000 degrees of freedom, and the modal model consisted of 132 modes. The transformation from the physical coordinates model (described in the nodal degrees of freedom) into modal coordinates (described in the modal displacements) is given in the Appendix A.

The finite element model was developed for the structure free rotating with respect to the elevation and azimuth axes, thus it had two natural frequencies at zero. The modal data from the finite element model included modal masses, stiffness, and symmetric and antisymmetric mode shapes. Modal damping was assumed to be the same for all modes, namely 0.01 (1%). The damping alternative was introduced based on the DSN antenna available information. For example, for the 70-meter DSN antenna the measured damping of the fundamental mode was 1%, and the measured damping of the quadripod and subreflector was only 0.5%. Since the subreflector arm dynamics is more dominant for the NRAO antenna, it was necessary to test the two possible damping values.

The structural model had 7 inputs: the torques of the elevation pinions 1, and 2, the torques of the azimuth pinions 1, 2, 3, 4, and the wind force input. The first six inputs were introduced to make possible the attachment of the elevation and azimuth drives to the structure. The last input, wind force, was used to simulate the wind disturbances acting on the antenna. The structural model had 18 outputs: elevation encoder angle and rate, azimuth encoder angle and rate, elevation and cross-elevation pointing, X,Y,Z subreflector displacements, X,Y,Z, feed displacements, rates of the elevation pinion 1 and 2, rates of the azimuth wheels 1, 2, 3, 4. The outputs were needed either to record the results of simulation, or to introduce the feedback loops, either in the rate-loop model or in the position-loop model.

The properties of the structural model were illustrated with the plots of magnitudes of the transfer functions from the elevation pinion torque input to the elevation and azimuth encoder rates (Fig.1a), and from the azimuth pinion torque input to the elevation and azimuth encoder rates (Fig.1b). They showed the zero natural frequency (or, alternatively, the integral behavior), since the transfer function from the elevation input to elevation output (or azimuth input to azimuth output) grow (20 dB/dec) as the frequency approaches zero. The lowest structural frequency excited by the azimuth pinion was about 0.6 Hz, while the lowest structural frequency excited by the elevation pinion was about 1.1 Hz. They will be later visible in the closed-loop simulations. The highest modeled frequencies were about 10 Hz.

In order to accelerate simulations the structural model was reduced, since many modes in the structural model are redundant. This excess is reduced by using the technique given in Refs.[2], [3], [4]. The method is summarized in the Appendix B. The importance of each mode is evaluated by the positive index called the Hankel singular value. It depends on the structural properties, as well as the locations of sensors and actuators. The Hankel singular values of the GBT structure are plotted in Fig.2. Nineteen modes characterized by the nineteen largest Hankel singular values were chosen for the reduced structural model. The transfer functions of the reduced structural model are shown in Figs.3a and 3b. They are very close to the ones of the full model in Figs.1a and 1b.

3. Rate Loop Model

The rate loop model consisted of the structural model, two elevation drive models and four azimuth drive models. The block diagram of the drive model was in Fig.4 which was the same for each drive, although had different values of the parameters. In this diagram, G1 and G2 described amplifiers and compensation electronics, G3 described the motor, and G4 described the gearbox. Detailed modeling of each component was described in Ref.[2].

The block diagram of the rate loop model was given in Fig.5, where for the sake of simplicity, each block represents two drives.

4. Position Loop Model

The feedback loops between the encoder output and the rate input of the rate loop model were introduced as in Fig.6, separately for elevation and azimuth axes. The proportional-and-integral (PI) controller in each feedback loop was introduced. The position loop equations were derived in Ref.[2]. The controller parameters are given in Table 1.

Table 1. Controller gains

	proportional gain	integral gain
elevation	1.0	0.6
azimuth	1.0	0.6

The step responses of the position loop model to elevation and azimuth commands were presented in Figs.7, and 8. Fig.7a showed the elevation encoder output due to the elevation step command, and Fig.7b showed the azimuth encoder output due to the elevation step command. Both figures indicated the lightly damped oscillations of frequency 0.75 Hz. Furthermore, in Fig.8a the azimuth encoder output due to the azimuth step command is presented, and

Fig.8b the elevation encoder output due to the azimuth step command is given. Again, both figures showed the lightly damped oscillations of frequency 0.75 Hz.

Similar conclusions could be drawn from the transfer function plots, in Figs.9, and 10. They showed good tracking properties for frequencies not exceeding 0.1 Hz, and the significant resonance peak at the frequency 0.75 Hz.

It is expected that the excess vibrations at the frequency 0.75 Hz could be reduced by the introduction of the acceleration limits at the antenna input. However, our experience with the DSN antennas showed that the best cure was the controller upgrade with the LQG gain as described in Ref.[5]. The upgrade reduced extensively the vibrations induced by the commands, as well as the vibrations excited by wind.

5. Wind Model

The wind model was developed in a similar way as for the DSN antennas, see Ref.[2]. This model was developed based on the available data from Refs.[6], [7], [8], which contained the static wind pressure distribution on a paraboloidal dish. The data were obtained during the wind tunnel experiments. Recently, these data were confirmed with the field measurements on the 34-m DSN antenna, see Ref.[9]. The wind simulation model was developed using the assumption that the wind gust pressure distribution is similar to the steady-state distribution. This assumption was introduced due to the lack of the gust pressure profile. It can be justified by the fact that the gusts consists of 20% of the steady-state pressure, thus the total pressure profile is not significantly deteriorated by the gusts.

The pressure distribution was applied to the finite element model of the antenna dish, and the modal wind coefficients were obtained from the finite element model. These coefficients were used to determine the wind input in the modal structural model. The wind time-history were obtained for the antenna site using the experimental Davenport spectra, Refs.[10], [11]. A filter which approximated the Davenport spectrum was designed (see Fig.11a), and it produced the wind time history as in Fig.11b.

Front wind gusts (from y-direction, see Fig.12), and side wind gusts (from x-direction, see Fig.12) acting on antenna at 60 deg elevation were simulated.

The results of the simulations of the elevation pointing error due to the front wind gusts were shown in Fig.13 for the antenna damping of 0.5%, and of 1%. The cross-elevation pointing error was zero, due to the symmetry of the structure and the loading. The wind blew into antenna dish, while the dish elevation angle was 60 deg. The simulation results showed that the drop in the damping increased the elevation error about 10%. In Figs.14a,b samples of the elevation pointing due to 40-mph front wind, and its spectrum, are plotted. They show a dominant mode at frequency 0.77 Hz.

The results of simulations of the side-wind gusts on the antenna are presented in Fig.15a,b, again for the antenna damping of 0.5% and 1.0%. They show small elevation error, and a significant cross-elevation error. This error is caused predominantly by exciting the 0.6 Hz mode, as shown in the samples of the elevation and cross-elevation pointing due to 40-mph side wind, and their spectra, in Fig.16a-d. They show a dominant mode at frequency 0.6 Hz. The subreflector tip displacement in the x, y, and z directions is plotted in Figs.17a-c, showing again the vibrations at 0.6 Hz.

The figures show a comparatively small error for the front will. It is due to the antenna configuration at 60 deg elevation, as in Fig.12. This configuration results in the smallest wind resistance of the antenna.

The results of simulations are summarized in Table 2, where the pointing errors in arcsec, and subreflector displacements in inches are given for the 50 mph front and side wind. The pointing is specified separately for the steady-state wind loads, for wind gusts (standard deviation of the pointing time history), and for the total load, which is obtained as the rms of the steady-state pointing error and the error due to gust loads. Table 3 compares results of our simulations and the results presented in the Loral Technical Memo, Ref.[12]. The Loral results, obtained for the 7 m/sec wind were re-scaled to the 50 mph wind (the "quadratic law" was applied, the scale was 10.27). The results show our lower estimates for the front wind, and higher estimates for the side wind.

Table 2. 50 mph wind action for the antenna at 60 deg elevation

	front, steady	front gusts(1)	front total(2)	side steady	side gusts(1)	side total(2)
EL pointing, arcsec	12	13	18	3.5	1.6	3.9
XEL pointing, arcsec	0	0	0	171	83	190
subrefl. x-displ., in.	0.0	0.3	0.3	3.9	0.8	4.0
subrefl. y-displ., in.	1.8	0.9	2.0	0.1	0.3	0.3
subrefl. z-displ., in.	0.4	0.4	0.6	0.1	0.1	0.2

(1) standard deviation of the time history

(2) root-mean-square of steady wind and gusts

Table 3. Comparison of the total pointing error estimate for 60 deg antenna elevation and 50 mph wind

	front, JPL	front, Loral	side, JPL	side, Loral
EL pointing, arcsec	18	32	4	5
XEL pointing, arcsec	0	0	190	125

In conclusion of the wind simulation study it is reminded that the following were the limitations of the analytical wind model:

1. The wind pressure distribution of the steady-state wind was used for the wind gust analysis (the wind *gust* pressure on the antennas was not available).
2. The wind pressure was distributed on the dish only (no wind tunnel data

were available for the wind pressure distribution on the alidade, arm, subreflector, etc.).

3. Only two directions of wind were considered: direction along the elevation axis, and the horizontal direction orthogonal to it.

6. Feedforward Controller

The tracking accuracy of fast moving objects can be improved if a PI servo is augmented with a feedforward loop, as shown in Fig.18. The feedforward loop contains the differenciator, see Ref.[2], thus its output is the command rate. The improved performance is observed in the closed-loop transfer function (Fig.19a,b for azimuth and elevation encoders due to azimuth command input, and Fig.20a,b for azimuth and elevation encoders due to elevation command input) when compared with the same transfer functions for a system without the feedforward gain, Figs.9 and 10. The figure shows that for frequencies up to 0.6 Hz the system with the feedforward gain has improved tracking properties when compared with the system without feedforward gain (the magnitude of the transfer function from elevation-to-elevation and azimuth-to-azimuth is equal to 1, and the cross-coupling from elevation-to-azimuth and from azimuth-to-elevation is small). The troubles are for higher frequencies, where the tracking properties deteriorate, and the cross-coupling is high. As a result, any sharp change in the command may cause excessive vibrations of the telescope.

The elevation and cross-elevation pointing transfer functions are shown in Fig.21a,b. They also show good tracking performance, similar to the encoder performance. However, the cross-elevation pointing model was not complete, which was visible in the cross-elevation transfer function (from azimuth input). For a complete model and for low frequencies the magnitude of this transfer function should be equal to 1. Actually, it was smaller than 1. It was corrected by re-scaling the model to obtain 1 for low frequencies.

The improved tracking properties are confirmed by tracking simulations with trajectories as these in Fig.22a,b. The maximal rates of these trajectories are 0.6 deg/sec in azimuth, and 0.3 deg/sec in elevation, see Fig.23a,b. The telescope with the feedforward loop and proportional gain $k_p=1.0$ and integral gain $k_i=0.6$ in azimuth and elevation was simulated. Servo errors are shown in Fig.23a,b, and the maximal error was 7 arcsec in azimuth, and 4 arcsec in elevation. Pointing errors are shown in Fig.24a,b, where the same maximal errors are found. Again, the cross-elevation response show small inaccuracies in the cross-elevation pointing model. The cross-elevation pointing should approach zero for time $t>120$ sec, similar to the azimuth servo error in Fig.23a. Instead, it shows a constant bias of about 7 arcsec, see Fig.24a.

Despite the increased sensitivity to the command inputs, the disturbance rejection of the antenna with feedforward gain remains the same as that for the antenna without feedforward gain, Ref.[2]. Thus the pointing errors due to wind gust disturbances are comparable with the results obtained for the PI servo.

7. Nonlinear Dynamics

The non-linear dynamics is observed when the rate and/or the acceleration limits are violated. The rate limits are 0.67 deg/sec in azimuth, and 0.33 deg/sec in elevation; acceleration limits are 0.2 deg/sec^2, both in azimuth and elevation. The limits are typically violated in a slewing mode (when a position offset is applied) or when the target and the initial position of the antenna do not coincide so that at the in the initial tracking stage the target trajectory is acquired. Both scenarios are conveniently illustrated when the large enough step command (such as 1 deg) is applied. In this scenario large overshoots are expected. In order to avoid large overshoots in the non-linear step responses, a command pre-processor, as developed by PCD, is applied.

The closed-loop antenna performance with the command pre-processor was simulated. The responses to azimuth step command of 1 deg are shown in Figs.26, 27, and 28, and to elevation step command of 1 deg are shown in Figs.29 and 30. Note that the cross-coupling from elevation to azimuth is not observed, due to the symmetry of the structural model. Figs.26a,b show small (10 mdeg) azimuth encoder overshoot to the azimuth step command of 1 deg. Similarly, Figs.27a,b show small (10 mdeg) overshoot in cross-elevation pointing, but this response has longer lasting oscillations. Figs.28a,b present the cross-coupling in the elevation encoder and elevation pointing. Both are smaller than 2 mdeg, and the elevation pointing variations more intensive. Quite similar results were obtained for the elevation step command.

The command as in Fig.31 was considered for simulations, to review the performance of the antenna for this often used scenario. Fig.31 shows the command in azimuth (dashed line) and the response at the azimuth encoder (solid line). The command rate is sidereal (0.0042 deg/sec) with rapid changes at max. rate (0.67 deg/sec). PCD preprocessor was included in the simulations. Fig.32 shows the azimuth encoder error for this simulation, and Fig.33 the cross-elevation error. Oscillations are quite large in the latter case.

The command in elevation (dashed line) and the response at the elevation encoder (solid line) are shown in Fig.34. The command rate is sidereal (0.0042 deg/sec) with rapid changes at max. rate (0.33 deg/sec). PCD preprocessor was included in the simulations. Fig.35 shows the elevation encoder error for this simulation, and Fig.36 the elevation error. Oscillations are small.

Finally, the 7-m/s (15.6-mph) side wind (along the elevation axis) was simulated with the non-linear model, and the results are shown in Fig.37 (encoder errors) and Fig.38 (pointing errors). The errors are similar to the ones obtained with the linear model, since neither the rate nor acceleration limits were violated in this case. Thus for 7-m/s wind, which is 6-m/s steady wind gusting to 7-m/s, we obtained 10.6 arcsec pointing error due to steady wind and 8.1 arcsec rms error due to gusting. The rss gives 13.3 arcsec of total error due to wind.

The friction and stiction phenomena of rolling azimuth wheels were modeled and the simulation results follow. The friction/stiction torques are taken from PCD data for the alidade case. The simulations were performed for 1 deg step command in azimuth, with the preprocessor. Fig.39 shows the azimuth wheel rotation, where periods of stiction (no movement is visible). Fig.40 shows the azimuth encoder angle, which shows additional small oscillations on top of the sticking movement (note that the wheels stick, while the structure at the encoder can move, not to mention RF beam in cross-elevation, which is shown in the next figure). Fig.42 shows the cross elevation pointing in the step response with friction. Again the vibrations at .7 Hz are visible.

Simulation of tracking at sidereal rate with friction in azimuth are also performed. In this case Fig.42 shows wheel rate, no stiction is observed. Fig.43 shows azimuth error at encoder, and the rate.

8. The Accuracy of the Antenna Analytical Model

The question arises concerning the accuracy of the simulation results of the antenna. The antenna servo model was developed using the finite element mode. The model size was reduced, but its accuracy was compared with the full model, giving close results. The wind model is based on the wind tunnel data Ref.[6], [7], and [8] confirmed by the field measurements, Ref.[9], and by the antenna wind model, Ref.[13].

The accuracy of the analytical model of the NRAO antenna could be ultimately evaluated only through the comparison of the simulation and the field data. For the obvious reason the field data for the NRAO antenna were not available at the moment. However, since the model of the NRAO antenna was developed in a similar way as the DSN antenna models, the comparison of the simulation and the field data for the DSN antenna (DSS-24) can give some insight into the accuracy of the simulation tools.

On May 25, 1994 the DSS-24 antenna was tested with the 10 mdeg step input commands, see Ref.[14], and the results were shown in Fig.44. The responses for the same step commands were also simulated with the DSS-24 analytical model, and were shown in Fig.45. They showed that the simulation results were close to the field data, however, they were not identical.

The more precise simulation results could be obtained for the antenna model which is obtained from the field test data rather than from the finite element formulation. For example, using the identification techniques the DSN antenna open-loop model was determined, and the closed-loop performance simulated, as in Ref.[5]. The azimuth trajectory, as in Fig.46 was tracked, and the servo errors, simulated and measured, were compared in Fig.47. This figure showed satisfactory precision of simulations. Thus, for the precise simulations it would be beneficiary to conduct tests, and to identify the NRAO antenna model using the field test data.

It was not a surprise that the analytical antenna model was inaccurate. The misalignment of the finite element model and test results was a common experience of structural analyst. For example, for the DSN antennas it has been observed that some natural frequencies were 10-12% off the measured ones. In spite of these inaccuracies one could determine the 'first cut' controller gains. These gains were used in the preliminary testing and could be corrected during the final tests.

9. Conclusions

1. The structural dynamics do not display any abnormal modes that should be of concern. The lowest simulated closed-loop structural resonance is at 0.68 Hz. This is above GBT Design Specification which is 0.5 Hz or better.

2. The axes control loops as designed by RSi/PCD perform to the requirement of the GBT specification. The rate loop is implemented in the hardware, and the position loop in the software, the latter includes PI controller, rate feed-forward, and command pre-processor. Both loops have the provision to be tuned in the field.

3. The command preprocessor, with the rate and the acceleration limits levels structural excitation and overshoot. The calculated overshoot was below 10 mdeg for large steps (1 deg or more). The preprocessor is activated only when the position error exceeds 0.044 degree, and this is field adjustable value.

4. The dry friction and stiction does not have significant impact on the antenna dynamics. Limit cycling amplitude is below 1 mdeg, and it does not improve the damping of the flexible oscillations.

5. The simulated settling time for one degree step is about 12 second for elevation, and 15 second for cross-elevation.

6. The worst case pointing performance of the GBT is for wind gusting along the elevation axis. The simulations for this wind direction at speed of 7 m/s (steady state and gusting) indicate an rms pointing error of 13.3 arcsecond in cross-elevation, and less than 1 arcsec in elevation. The GBT Design Specification is 14 arcsec, thus the requirement is met.

REFERENCES

1. Strain, D., "Optimization of 100-meter Green Bank Telescope," *JPL Document,* JPL 94-6, 1994.
2. Gawronski, W., and J.A. Mellstrom, "Control and Dynamics of the Deep Space Network Antennas," a chapter in *Control and Dynamic System,* vol.63, ed. C.T. Leondes, Academic Press, San Diego, CA, 1994.

3. Gawronski, W., and Juang, J.N., "Model Reduction for Flexible Structures," in: *Control and Dynamics Systems*, ed. C.T. Leondes, vol.36, Academic Press, San Diego, 1990, pp.143-222.
4. Gawronski, W., and Williams, T., "Model Reduction for Flexible Space Structures," *Journal of Guidance, Control, and Dynamics*, vol.14, No.1, 1991, pp.68-76.
5. Gawronski, W., Racho, C., and Mellstrom, J.A., "LQG and Feedforward Controllers for the Deep Space Network Antennas," *IFAC Symposium on Automatic Control in Aerospace*, Palo Alto, CA, 1994.
6. N.L. Fox, B. Layman, Jr., Preliminary Report on Paraboloidal Reflector Antenna Wind Tunnel Tests. *JPL Internal Memo*, CP-3, 1962.
7. N.L. Fox, Load Distributions on the Surface of Paraboloidal Reflector Antennas. *JPL Internal Memo*, CP-4, 1962.
8. R.B. Blaylock, Aerodynamic Coefficients for Model of a Paraboloidal Reflector Directional Antenna Proposed for a JPL Advanced Antenna System. *JPL Internal Memo*, CP-6, 1964.
9. Gawronski, W., and J.A. Mellstrom, "Field Verification of the Wind Tunnel Coefficients," *TDA Progress Report*, JPL Publication, No. 42-119, Nov. 1994.
10. A.G. Davenport, "The Spectrum of Horizontal Gustiness Near the Ground in High Winds," *Journal of Royal Meteorol. Society*, vol.87 (1961).
11. E. Simiu and R.H. Scanlan, *Wind Effects on Structures*, Wiley, New York (1978).
12. D.M. Kelly, "Pointing Accuracy," Loral Technical Memo No 52, of 11/10/92.
13. W. Gawronski, B. Bienkiewicz, and R.E. Hill, Wind-Induced Dynamics of a Deep Space Network Antenna. *Journal of Sound and Vibration*, vol.176, No.5, 1994.
14. W. Gawronski, and J.A. Mellstrom, Preliminary DSS-24 Servo Testing Results, JPL IOM 3324-94-90, June 22, 1994.

Appendix A. From the Finite Element to the State Space Model

The state-space model of a flexible structure was obtained from its finite element model, which consisted of the mass M $(m\times m)$, stiffness K $(m\times m)$, input B_o $(m\times s)$, output C_{oq} $(r\times m)$, C_{ov} $(r\times m)$ matrices, the input $u(t)$ $(s\times 1)$, and output $y(t)$ $(r\times 1)$. The input-output relationship was given by the following second-order differential equation

$$M\ddot{q}+Kq=B_o u, \qquad y=C_{oq}q+C_{ov}\dot{q} \tag{A1}$$

where q was the vector of structural displacements. Consider now a modal matrix Φ $(m\times p)$, $p\leq m$, which consisted of p eigenvectors ϕ_i (mode shapes), $i=1,\ldots,p$

$$\Phi=[\phi_1,\phi_2,\ldots,\phi_p] \tag{A2}$$

which diagonalize M and K

$$M_m=\Phi^T M\Phi, \qquad K_m=\Phi^T K\Phi \tag{A3}$$

i.e. M_m, K_m were diagonal $(p\times p)$ matrices of modal mass and stiffness. Introducing new variable q_m $(p\times 1)$, such that

$$q=\Phi q_m \tag{A4}$$

and left-multiplying (A1) by Φ^T, one obtained either

$$\Phi^T M\Phi\ddot{q}_m+\Phi^T K\Phi q_m=\Phi^T B_o u, \quad y=C_{oq}\Phi q_m+C_{ov}\Phi\dot{q}_m \tag{A5a}$$

or

$$M_m\ddot{q}_m+K_m q_m=\Phi^T B_o u, \quad y=C_{oq}\Phi q_m+C_{ov}\Phi\dot{q}_m \tag{A5b}$$

or

$$\ddot{q}_m + M_m^{-1} K_m q_m = M_m^{-1} \Phi^T B_o u, \quad y = C_{oq} \Phi q_m + C_{ov} \Phi \dot{q}_m \tag{A5c}$$

Denote $M_m^{-1} K_m = \Omega^2$, where Ω was a diagonal *(p×p)* matrix of natural frequencies *(rad/sec)*. At this stage a damping matrix Z was introduced, $Z = diag(\zeta_i)$, $i = 1, \ldots, p$, such that $2Z\Omega = M_m^{-1} D_m$, and D_m was a modal damping matrix (assumed to be known), so that from (A5c) the modal model was acquired

$$\ddot{q}_m + 2Z\Omega \dot{q}_m + \Omega^2 q_m = M_m^{-1} \Phi^T B_o u, \quad y = C_{oq} \Phi q_m + C_{ov} \Phi \dot{q}_m \tag{A6}$$

Define the state variable x as follows

$$x = \begin{bmatrix} x_1 \\ x_2 \end{bmatrix} = \begin{bmatrix} q_m \\ \dot{q}_m \end{bmatrix} \tag{A7}$$

then (A6) could be presented as a set of first order equations

$$\dot{x}_1 = x_2, \quad \dot{x}_2 = -\Omega^2 x_1 - 2Z\Omega x_2 + M_m^{-1} \Phi B_o u, \tag{A8a}$$

$$y = C_{oq} \Phi x_1 + C_{ov} \phi x_2 \tag{A8b}$$

or in the following form

$$\dot{x} = Ax + Bu, \qquad y = Cx, \tag{A9a}$$

where

$$A = \begin{bmatrix} 0 & I \\ -\Omega^2 & -2Z\Omega \end{bmatrix}, \quad B = \begin{bmatrix} 0 \\ M_m^{-1} \Phi^T B_o \end{bmatrix}, \quad C = [C_{oq} \Phi \quad C_{ov} \Phi] \tag{A9b}$$

was the sought state-space model in modal coordinates.

Appendix B. Reduction of the Structural Model

Consider a flexible structure with small damping and distinct poles in modal coordinates. For each mode, say mode i one can determine the index γ_i, which classifies its importance in the system dynamics (based on the applied inputs, and measured outputs. This index, called the Hankel singular value is determined as follows, see Refs.[3] and [4] for details. For a structure with m modes, matrix B has $2m$ rows, and C has $2m$ columns. Denote b as the last m rows of B, c_q as the first m columns of C, and c_r as the last m columns of C. Then b_i is the ith row of b, c_{qi} is the ith column of c_q, and c_{ri} is the ith column of c_r. Denote $\beta_i^2=b_i b_i^T$, $\alpha_{qi}=c_{qi}^T c_{qi}$, and $\alpha_{ri}=c_{ri}^T c_{ri}$, and $w_{bi}>0$, $w_{qi}>0$, $w_{ri}>0$, $i=1,\ldots,m$ the weighting factors.. The Hankel singular value for the ith mode is given in Ref.[3], and Ref.[4]

$$\gamma_i^2 = \frac{w_{bi}\beta_i \sqrt{w_{qi}^2\alpha_{qi}^2+w_{ri}^2\omega_i^2\alpha_{ri}^2}}{4\zeta_i\omega_i^2} \tag{B1}$$

Care should be taken when determining Hankel singular values. Units should be consistent, otherwise some inputs or outputs receive more weight in Hankel singular value determination than necessary. Consider for example the azimuth encoder reading in arcsecs, and the elevation encoder reading in degrees. For the same angle, the numerical reading of azimuth encoder is 3600 larger than elevation encoder reading, hence the elements for the azimuth output are much larger than those for elevation. On the other hand, some variables need more attention than others: pointing error and encoder readings are the most important factors in the antenna performance, hence their importance has to be emphasized in mode evaluation. For the reasons of consistency of units and importance of variables, the weighting factors w_{bi}, w_{qi}, w_{ri} are introduced. Typically, weights are set to 1.

For each mode the Hankel singular value is determined and used to decide on the number of modes in the reduced structural model. For the rigid body modes Hankel singular values tend to infinity, hence rigid body modes are always included in the reduced model.

Figures

Figures:

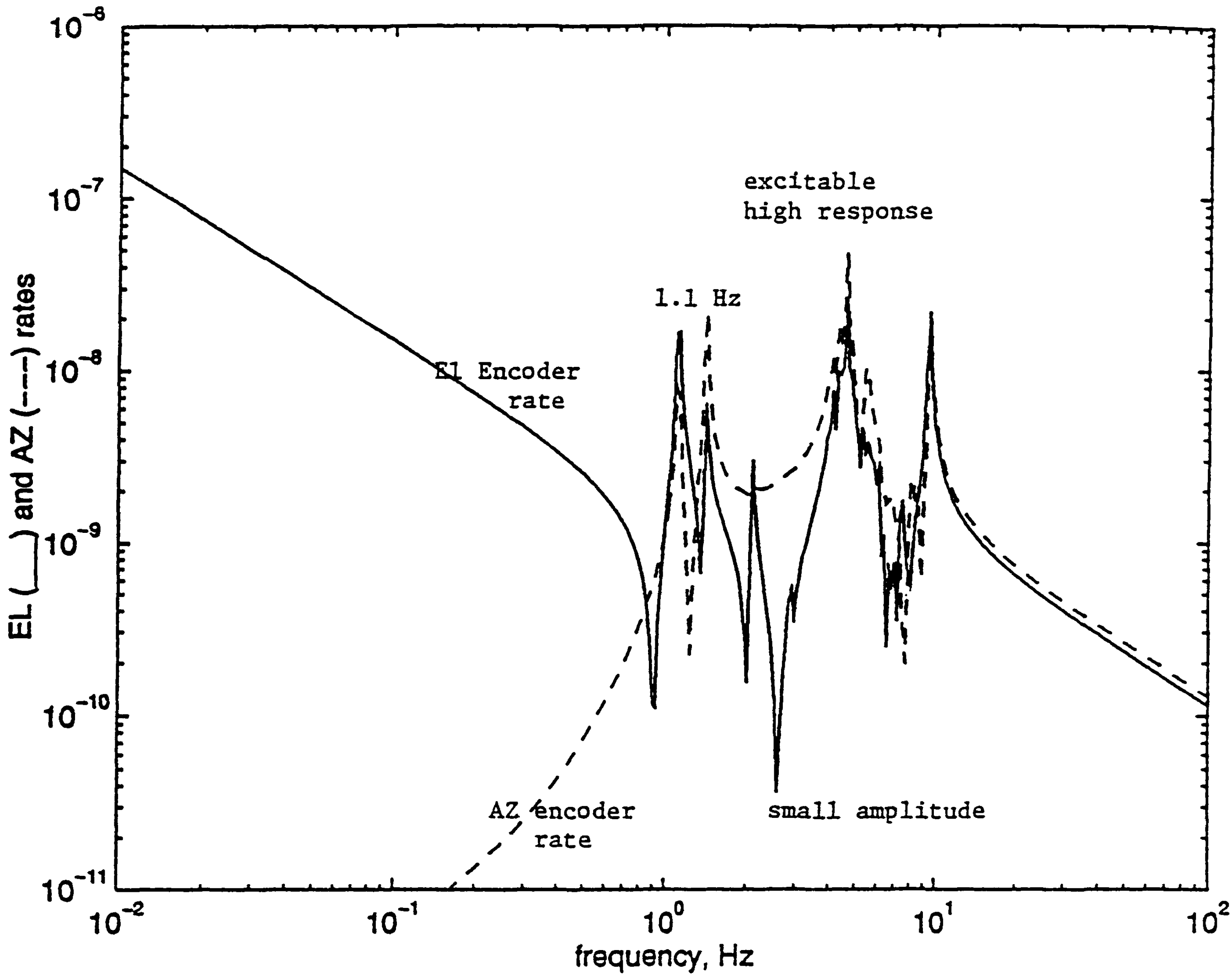

Fig.1a. Properties of the structural model (without gears and drives) illustrated by the magnitudes of the transfer functions from the elevation pinion torque input to the elevation and azimuth encoder rates,

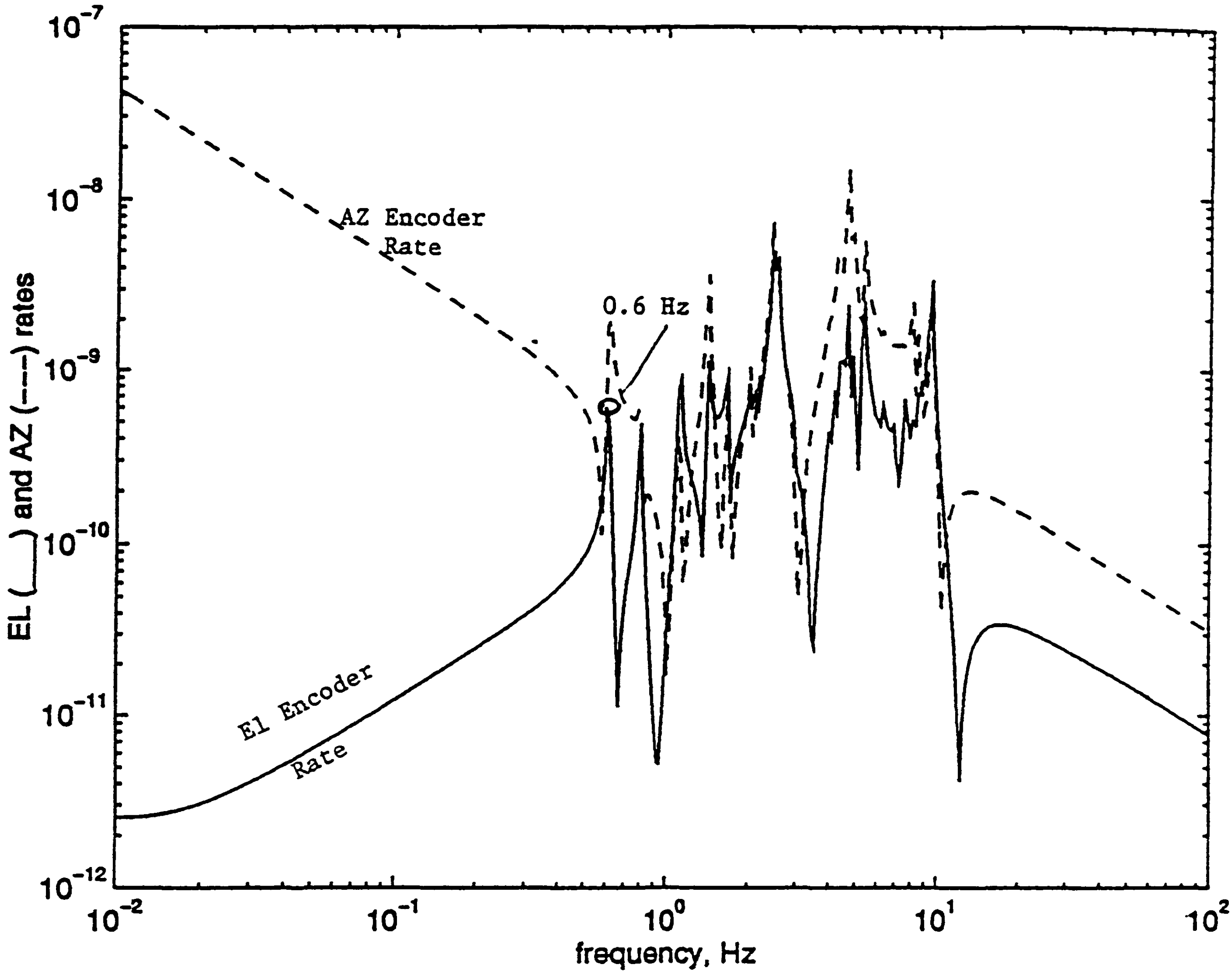

Fig.1b. Properties of the structural model (without gears and drives) illustrated by the magnitudes of the transfer functions from the azimuth pinion torque input to the elevation and azimuth encoder rates.

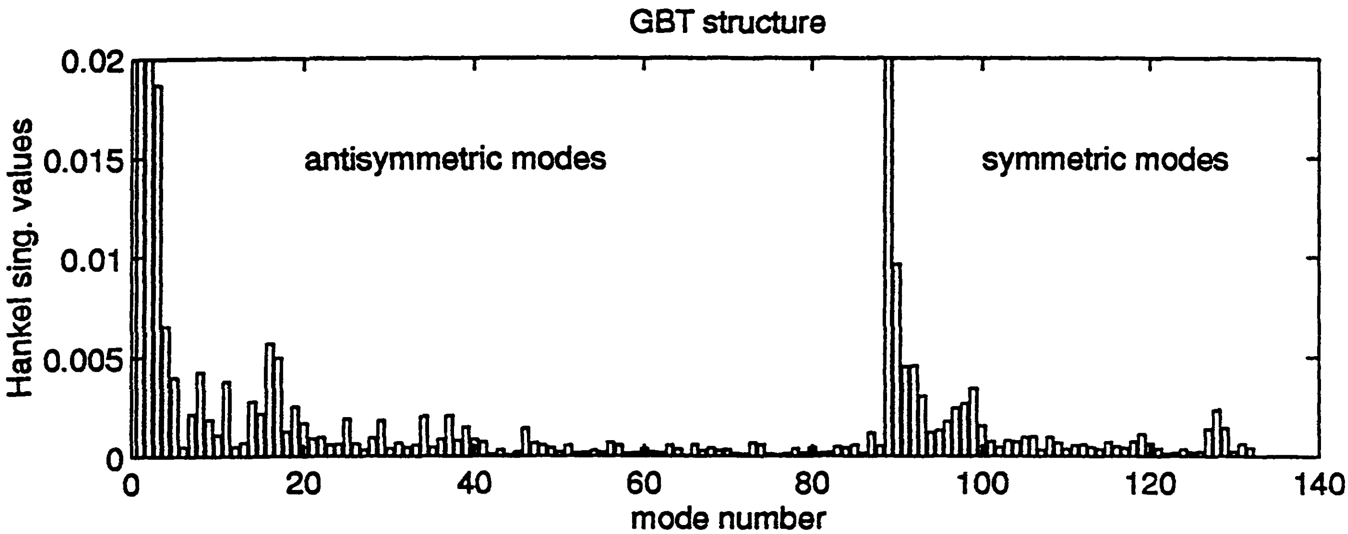

Fig.2. Hankel singular values of the GBT structure

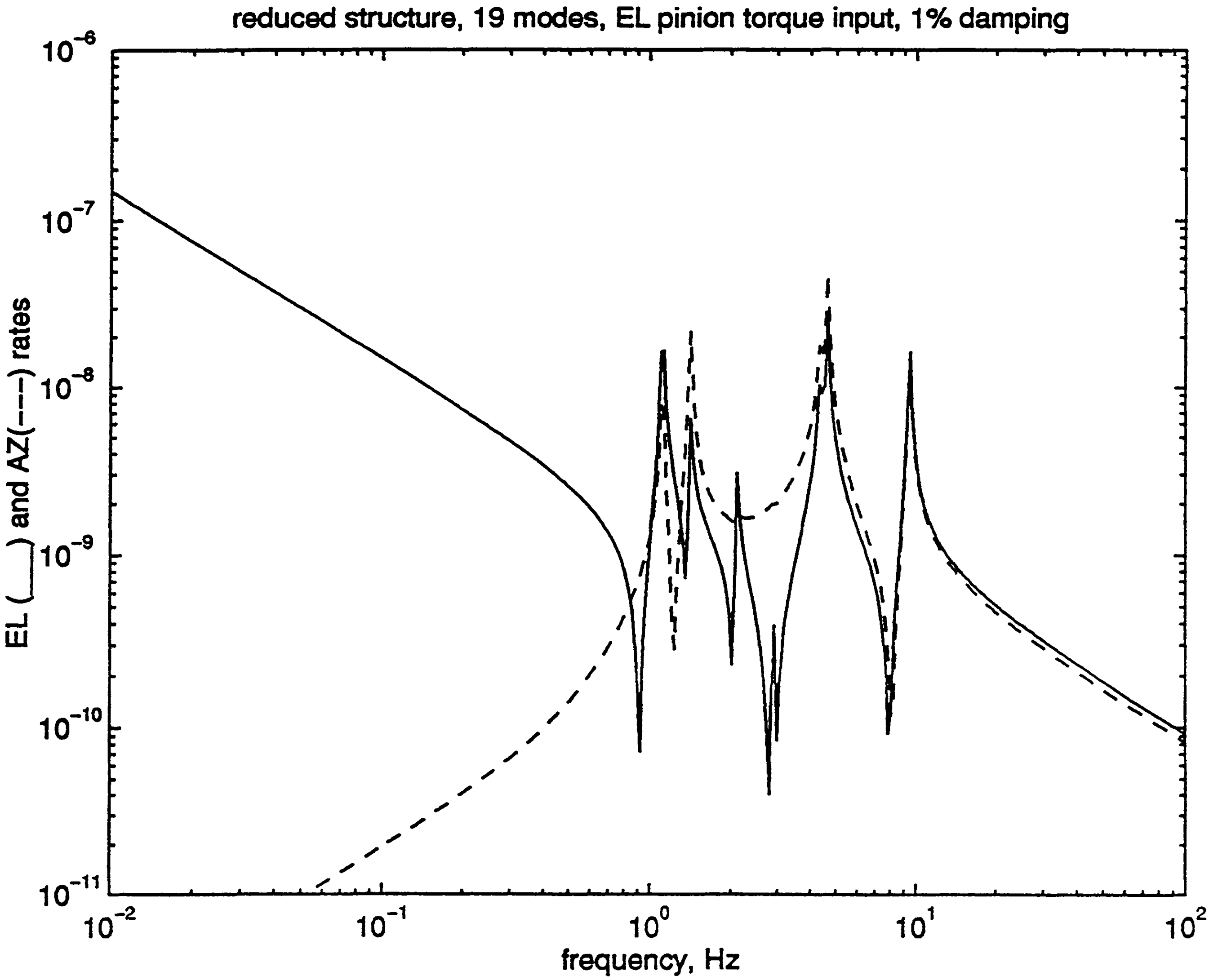

Fig.3a. Properties of the *reduced* structural model (19 modes) illustrated by the magnitudes of the transfer functions from the elevation pinion torque input to the elevation and azimuth encoder rates,

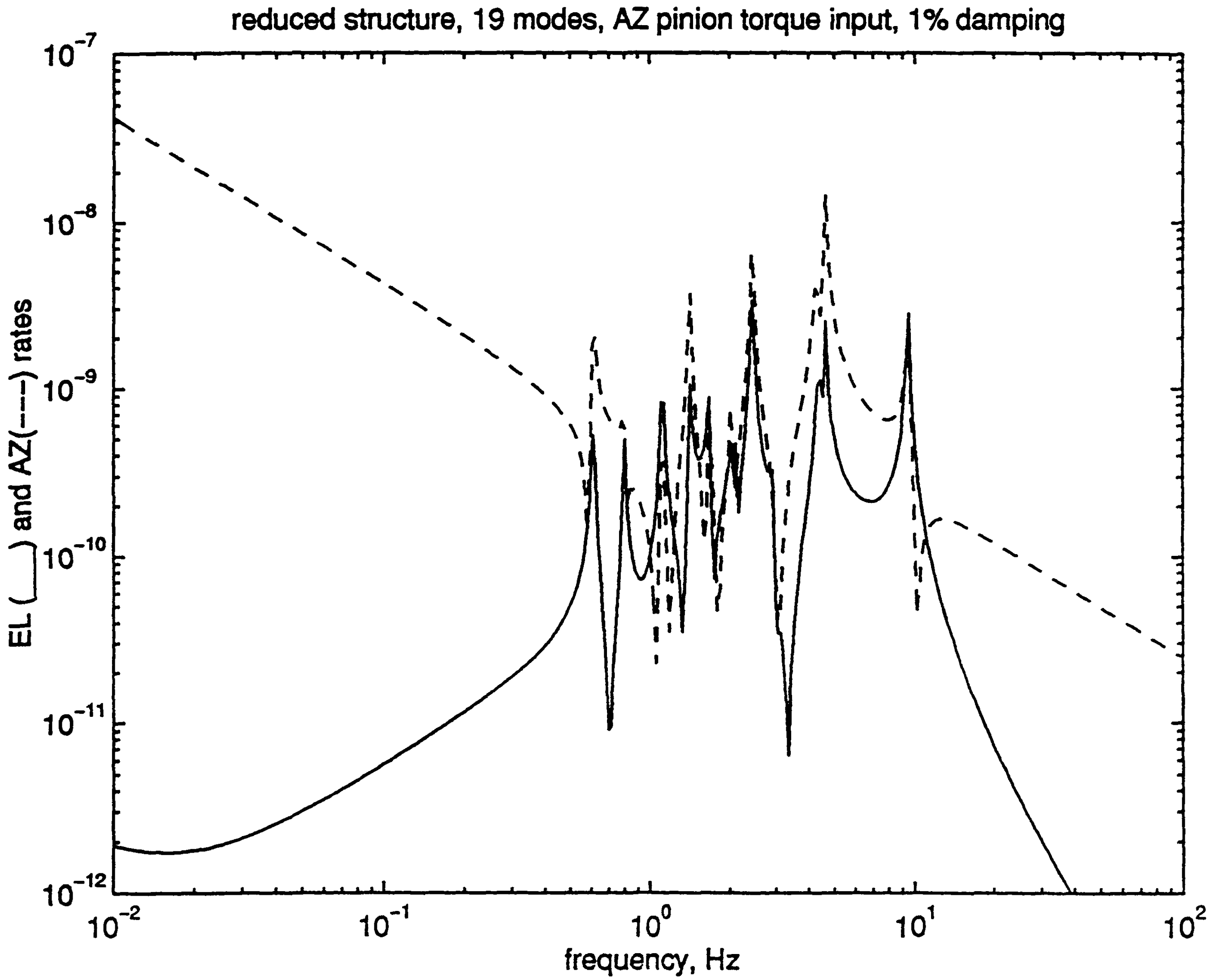

Fig.3b. Properties of the *reduced* structural model (19 modes) illustrated by the magnitudes of the transfer functions from the azimuth pinion torque input to the elevation and azimuth encoder rates.

RATE LOOP MODEL - DRIVE

(See Ref 2, Pg. 10 for the detailed modeling of each component.)

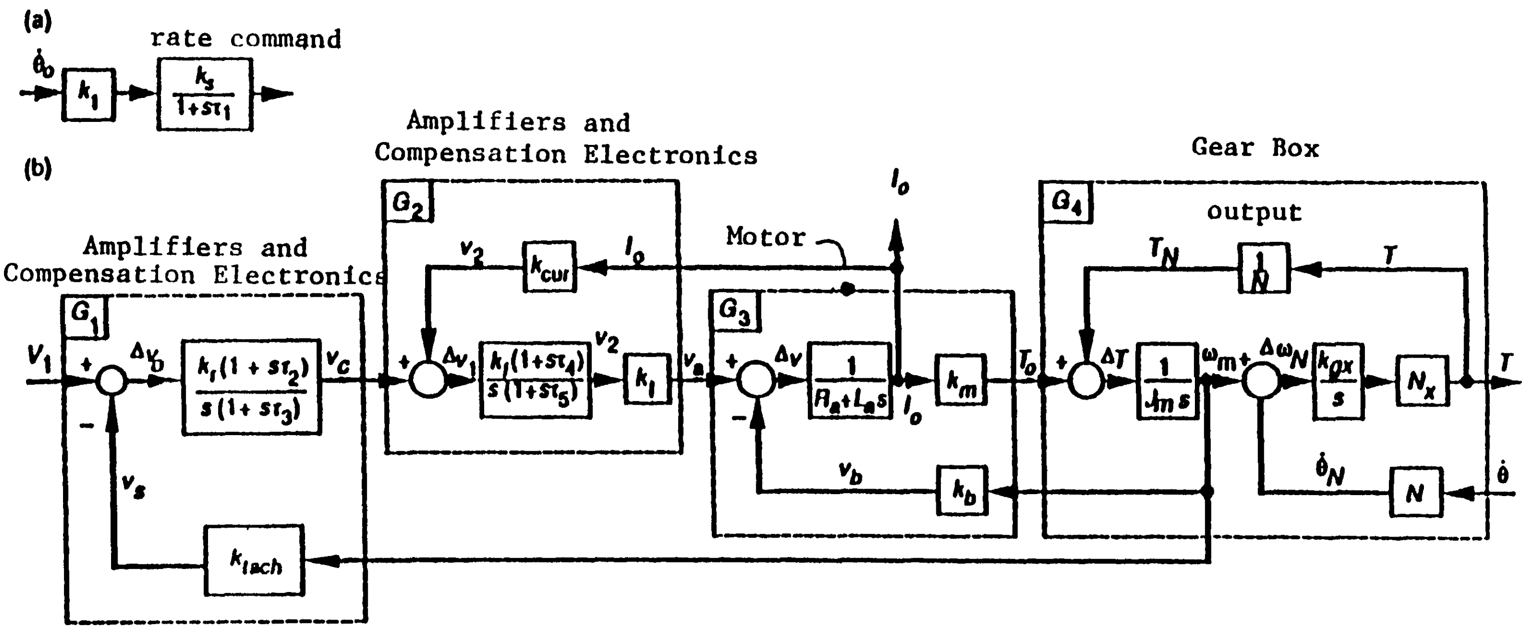

Drive Attached to the Structure

Fig.4. The drive model.

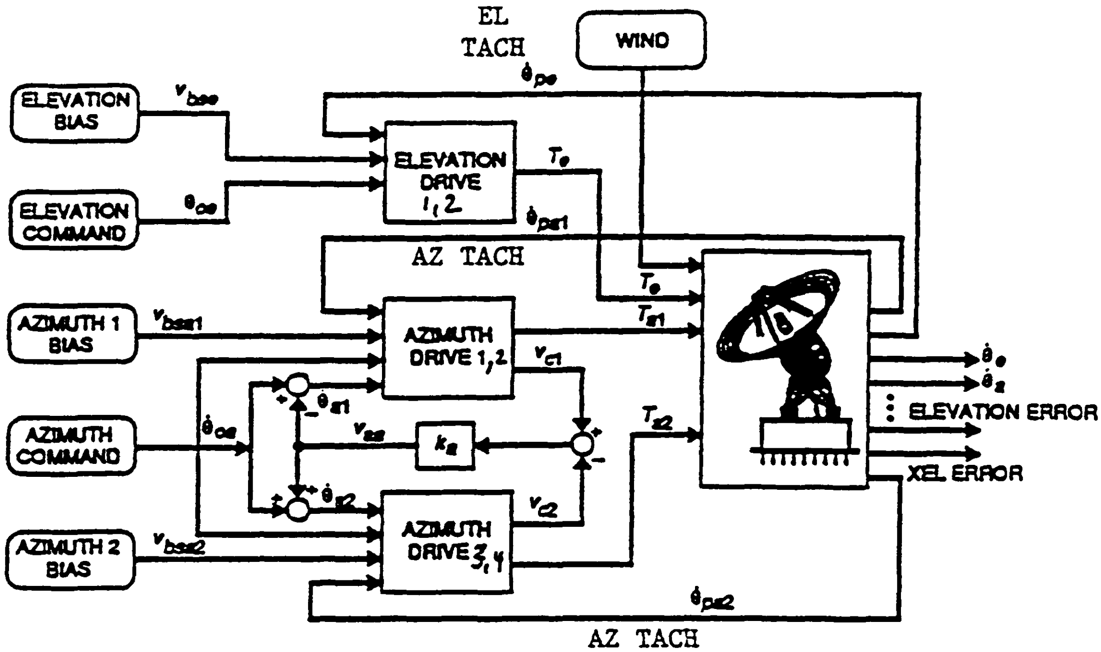

RATE LOOP MODEL

Incorporates Figure 4 and Structure

Fig.5. The rate-loop model.

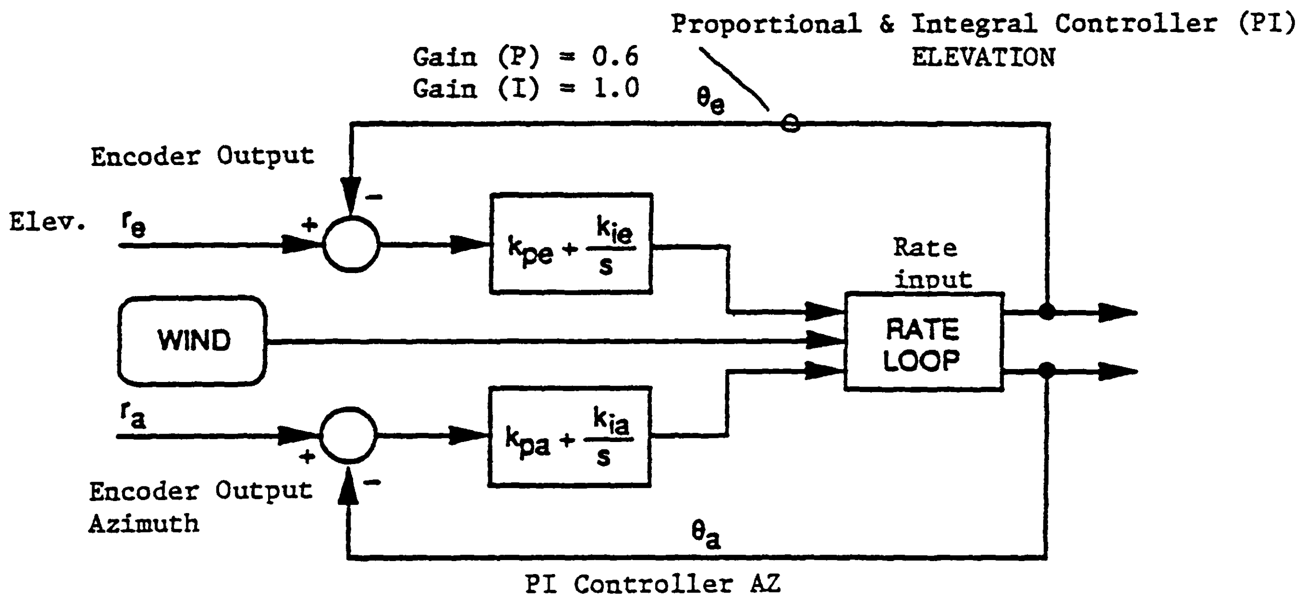

Fig.6. The position-loop model.

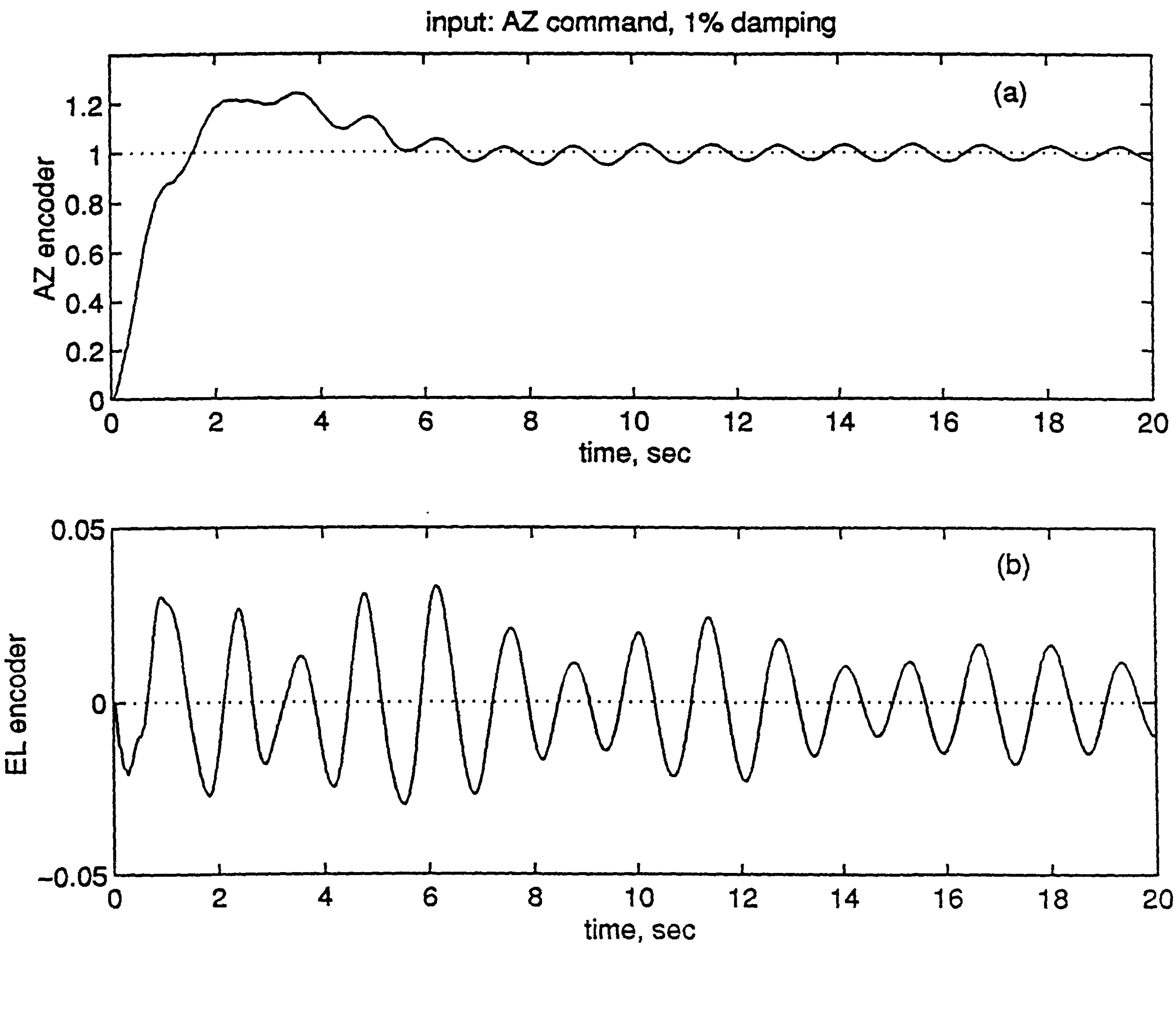

Fig.8. The responses of the position loop model to the azimuth step command, (a) azimuth encoder, (b) elevation encoder.

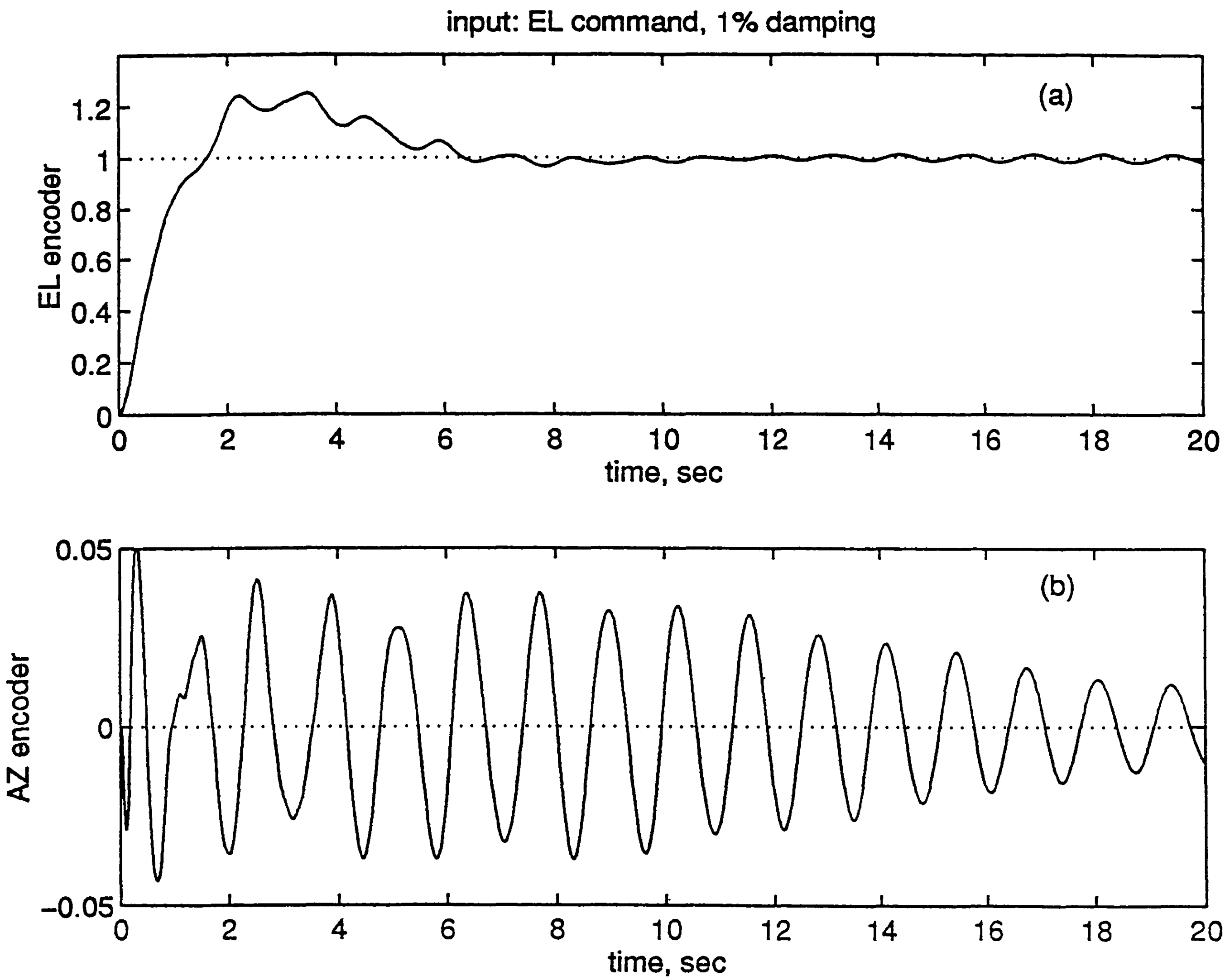

Fig.7. The responses of the position loop model to the elevation step command, (a) elevation encoder, (b) azimuth encoder.

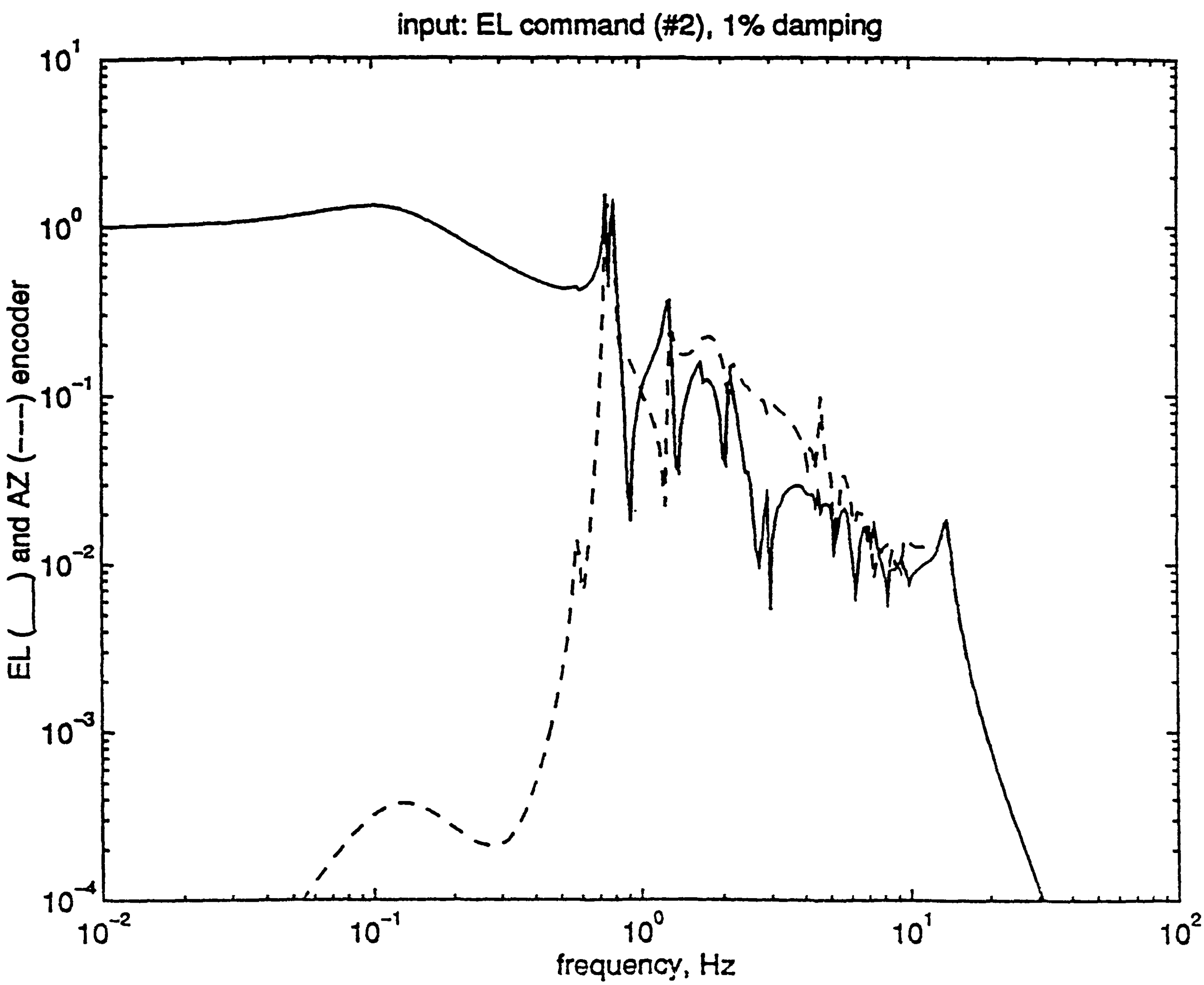

Fig.9. Magnitudes of the transfer functions, from the elevation command to elevation encoder (solid line), and from the elevation command to azimuth encoder (dashed line).

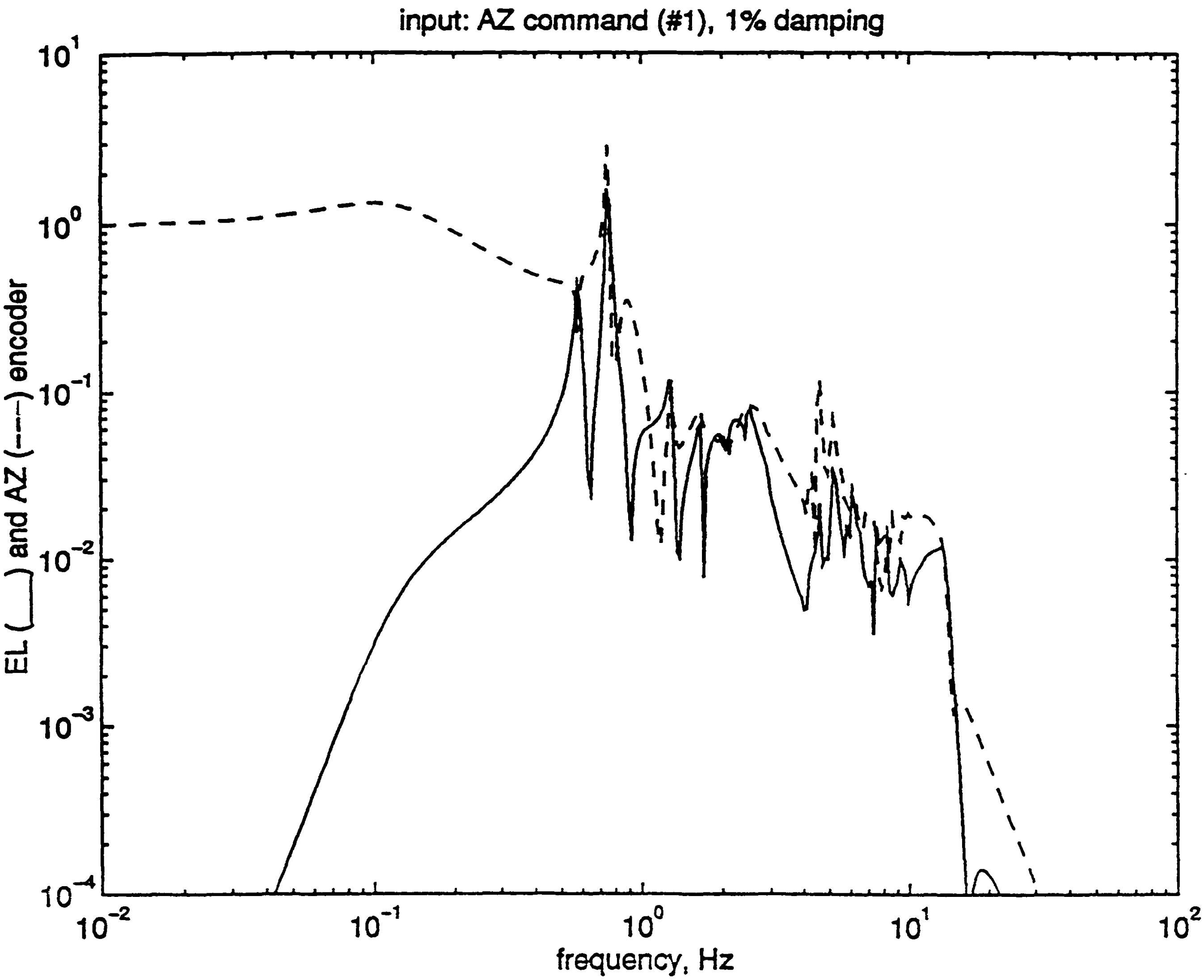

Fig.10. Magnitudes of the transfer functions, from the azimuth command to elevation encoder (solid line), and from the azimuth command to azimuth encoder (dashed line).

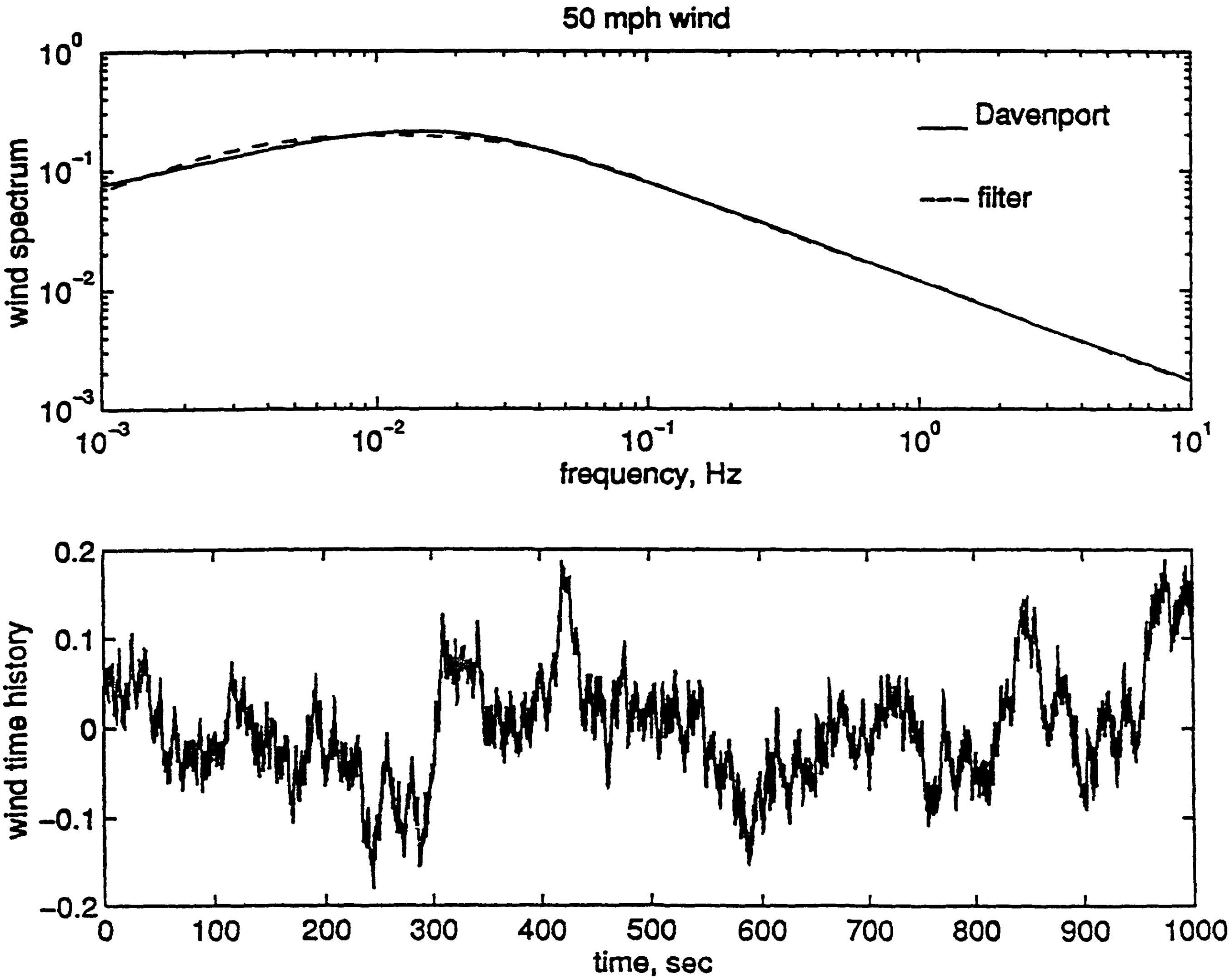

Fig.11. 50-mph wind model, (a) Davenport spectrum and wind filter spectrum, and (b) wind time history

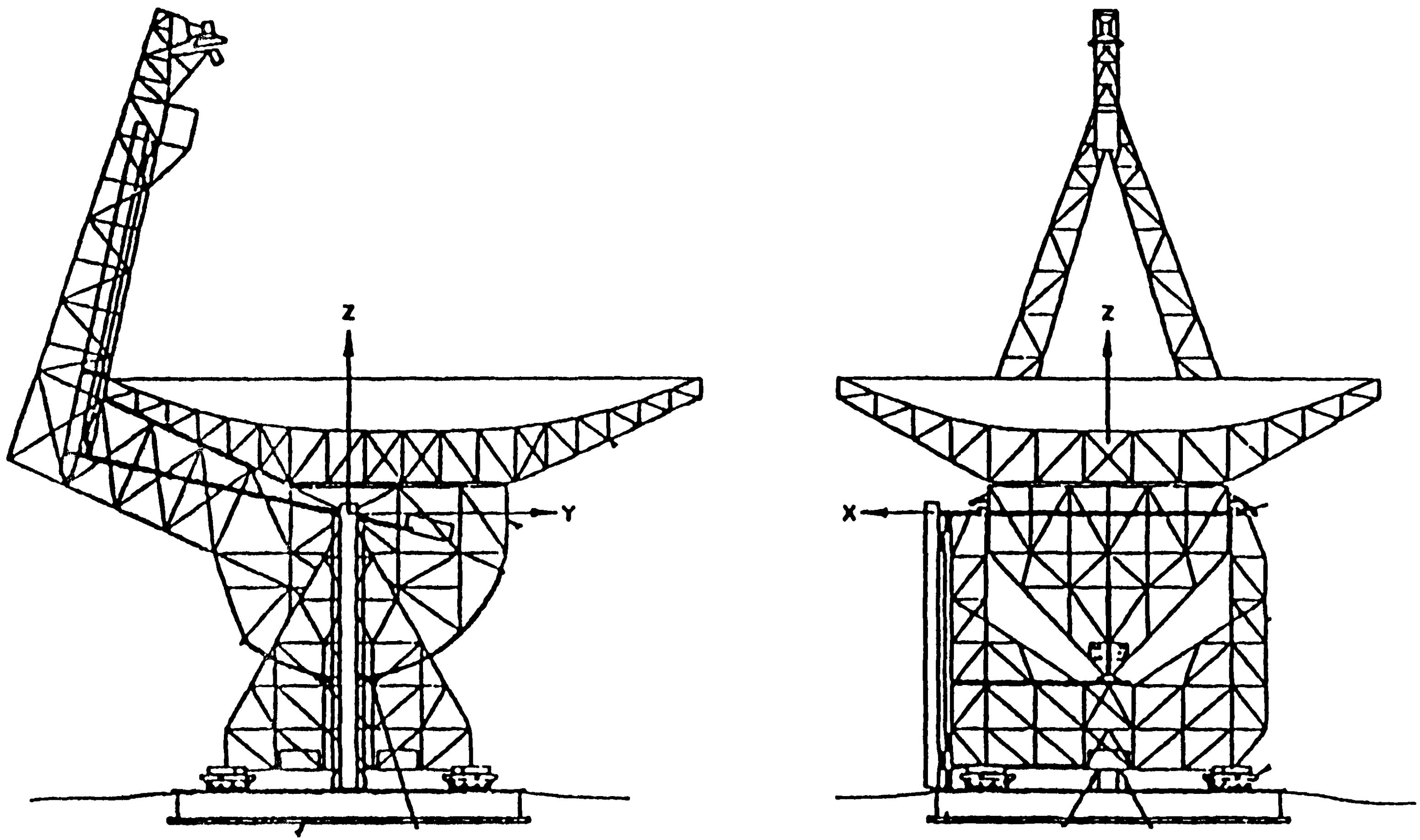

Fig. 12. Axis orientation of the GBT antenna.

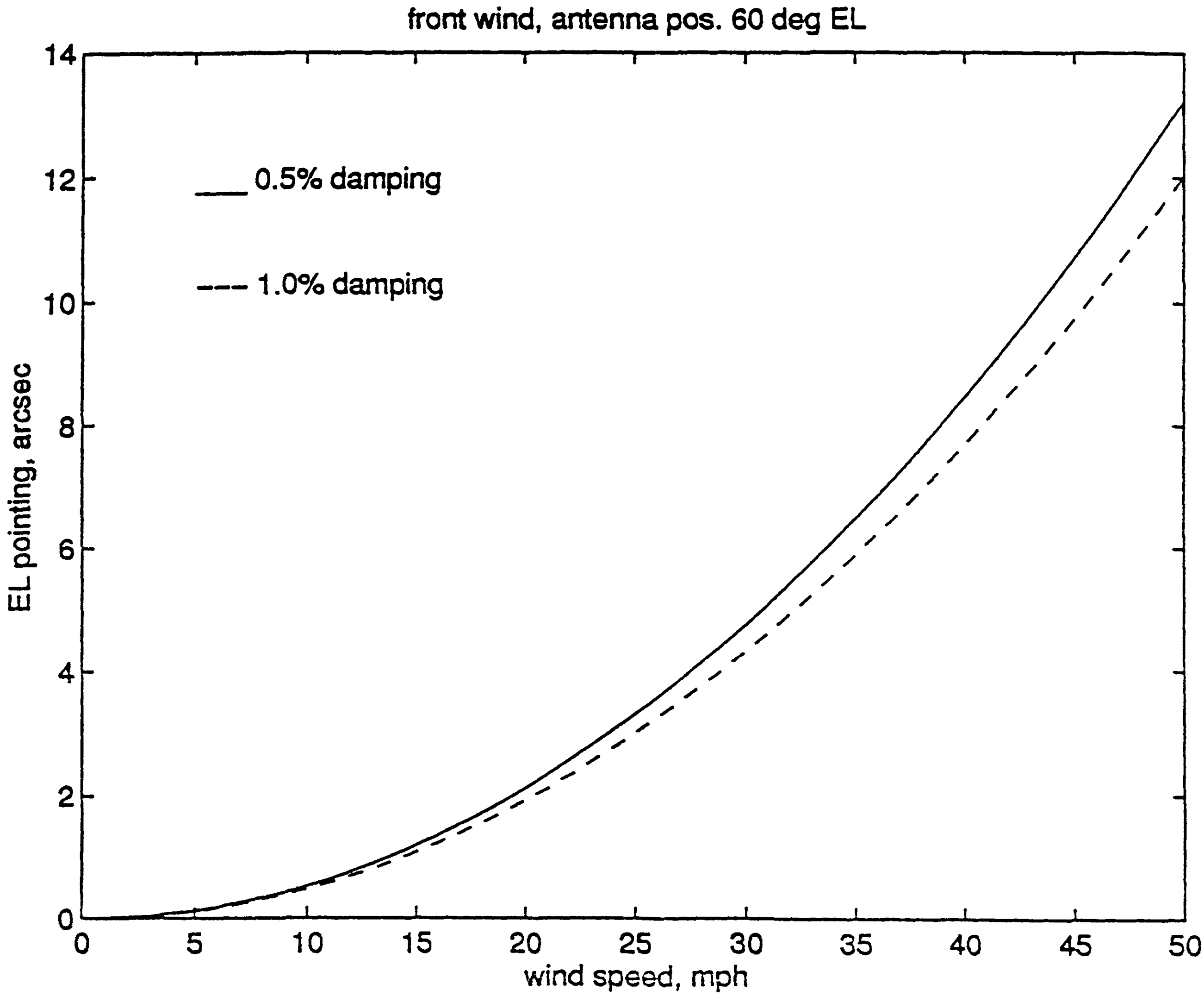

Fig.13. Elevation pointing error due to frontal wind gusts for the antenna damping of 0.5% and 1%.

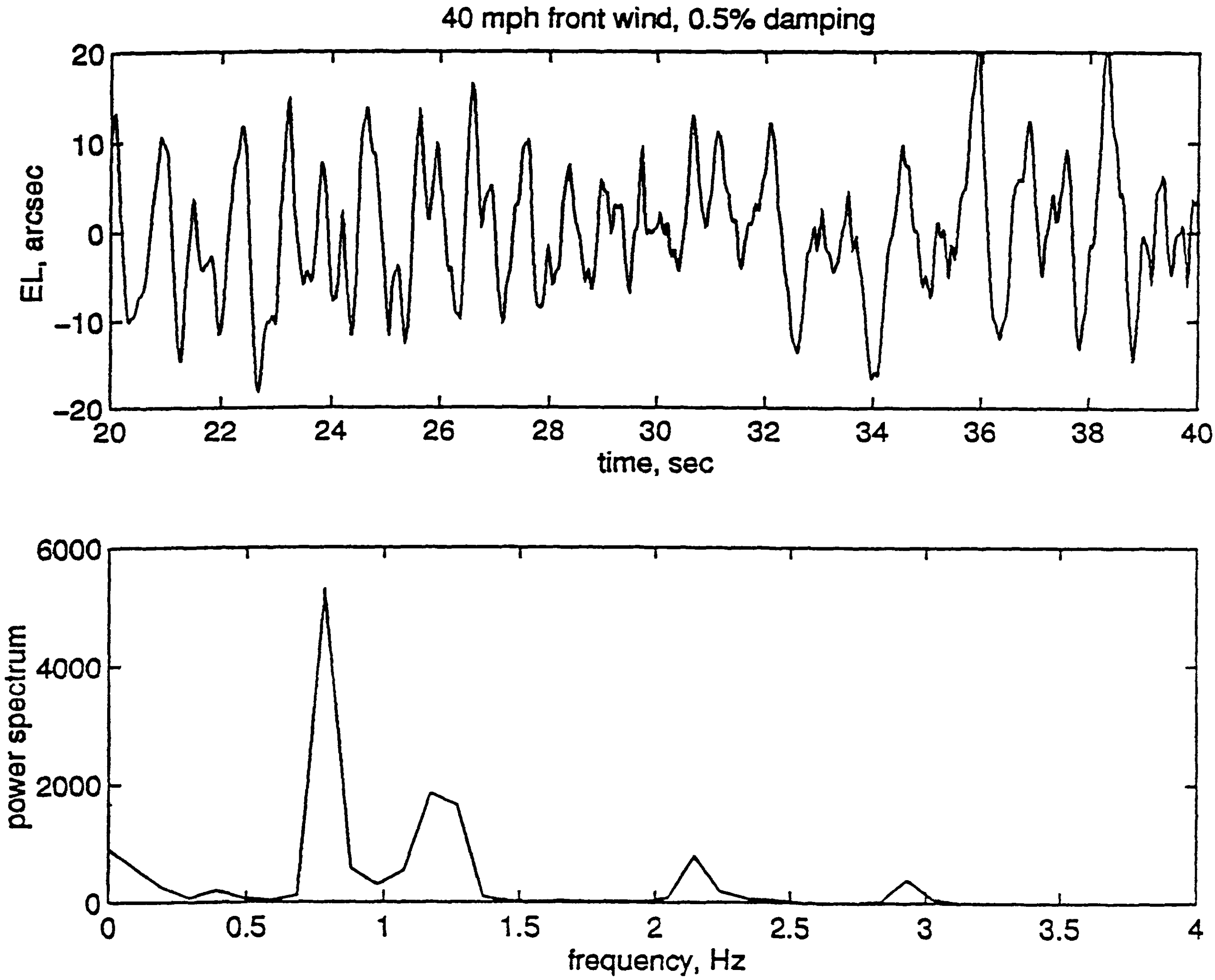

Fig.14. Detail of the simulations for the 40 mph frontal wind gusts, (a) elevation pointing error, (b) spectrum of the elevation pointing error.

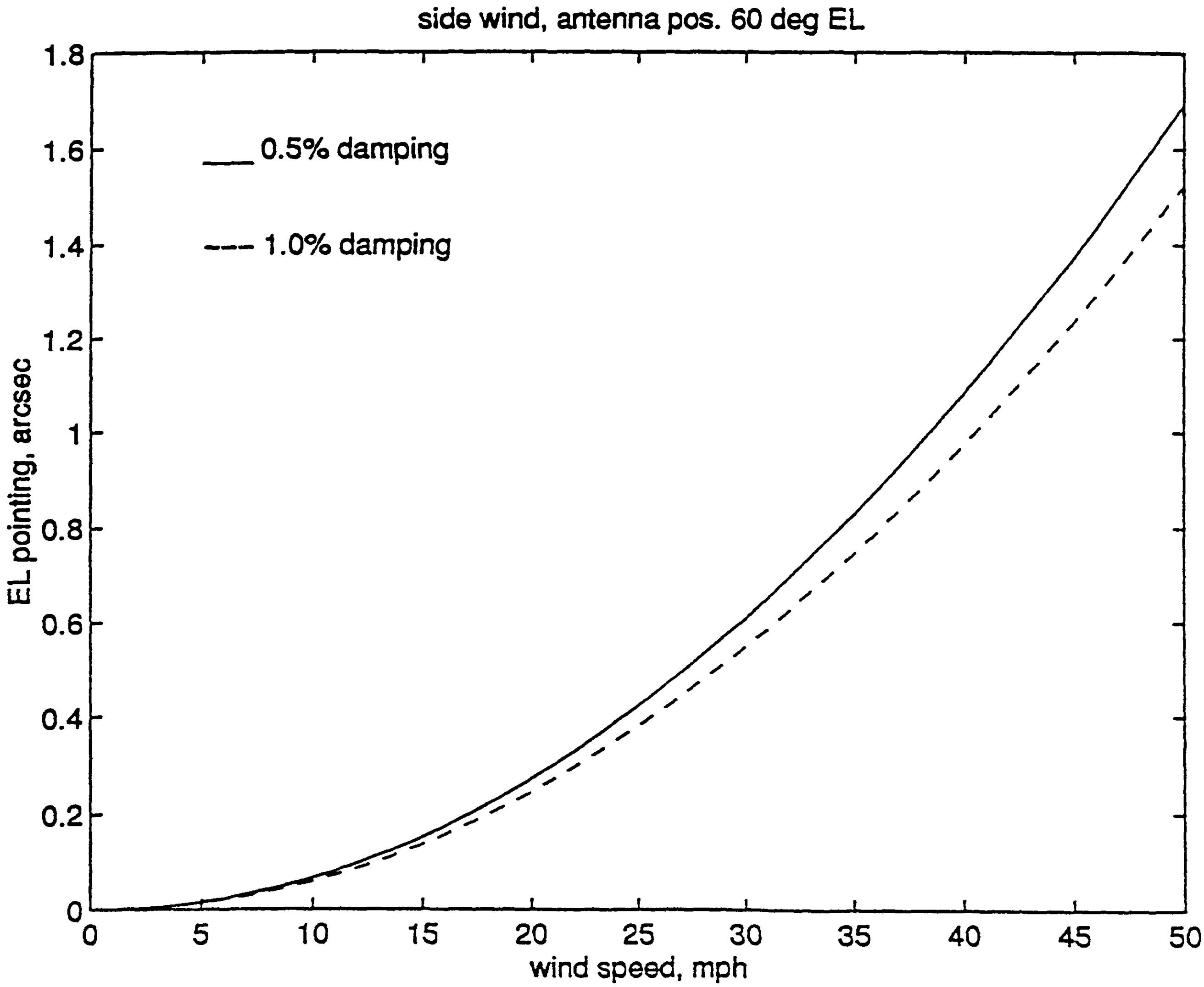

Fig.15a. Elevation pointing errors due to side wind gusts, for the 0.5% and 1% damping.

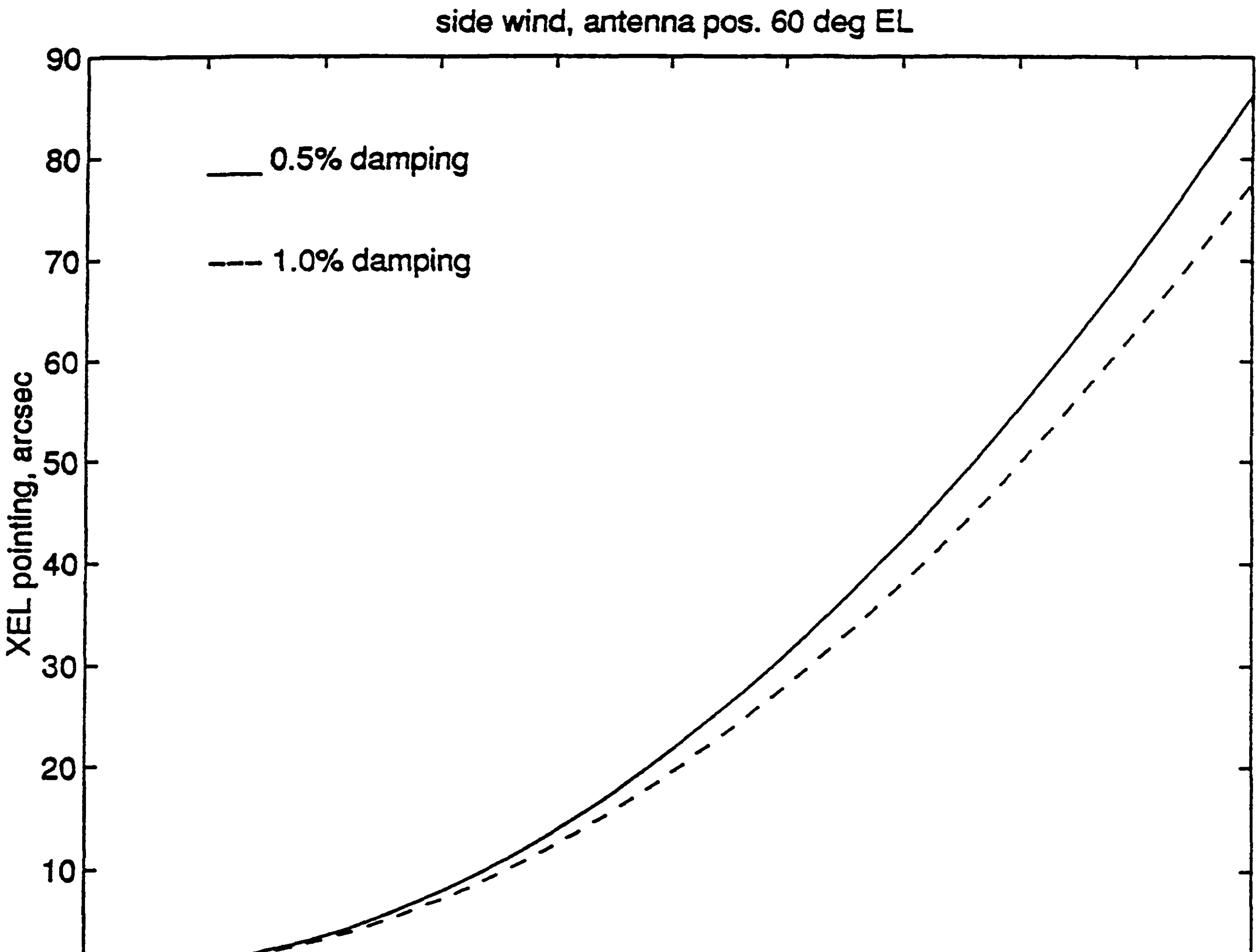

Fig.15b. Cross-elevation pointing errors due to side wind gusts, for the 0.5% and 1% damping.

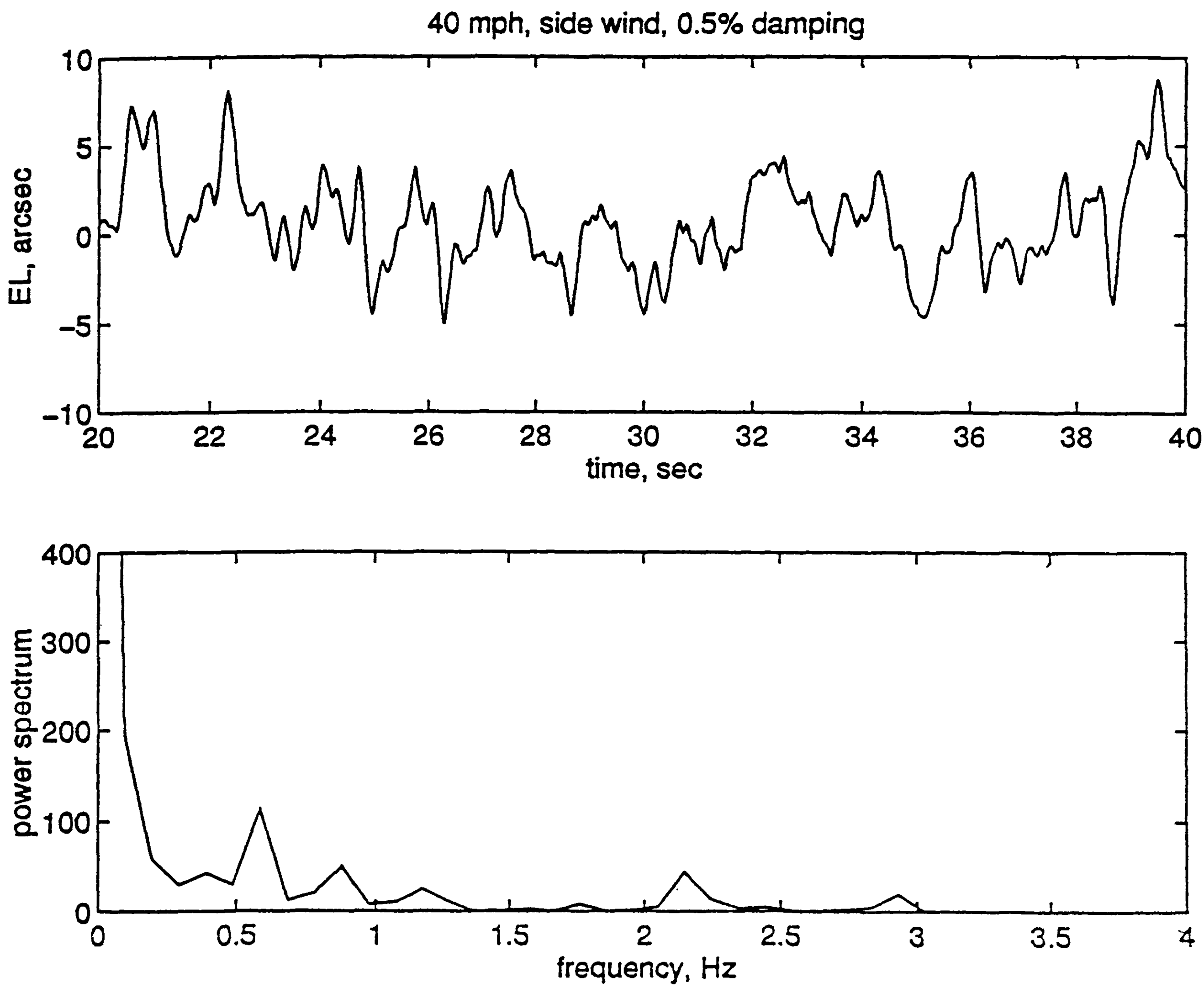

Fig.16a,b. **Detail of the simulations for the 40 mph side wind gusts, (a) elevation pointing error, (b) spectrum of the elevation pointing error.**

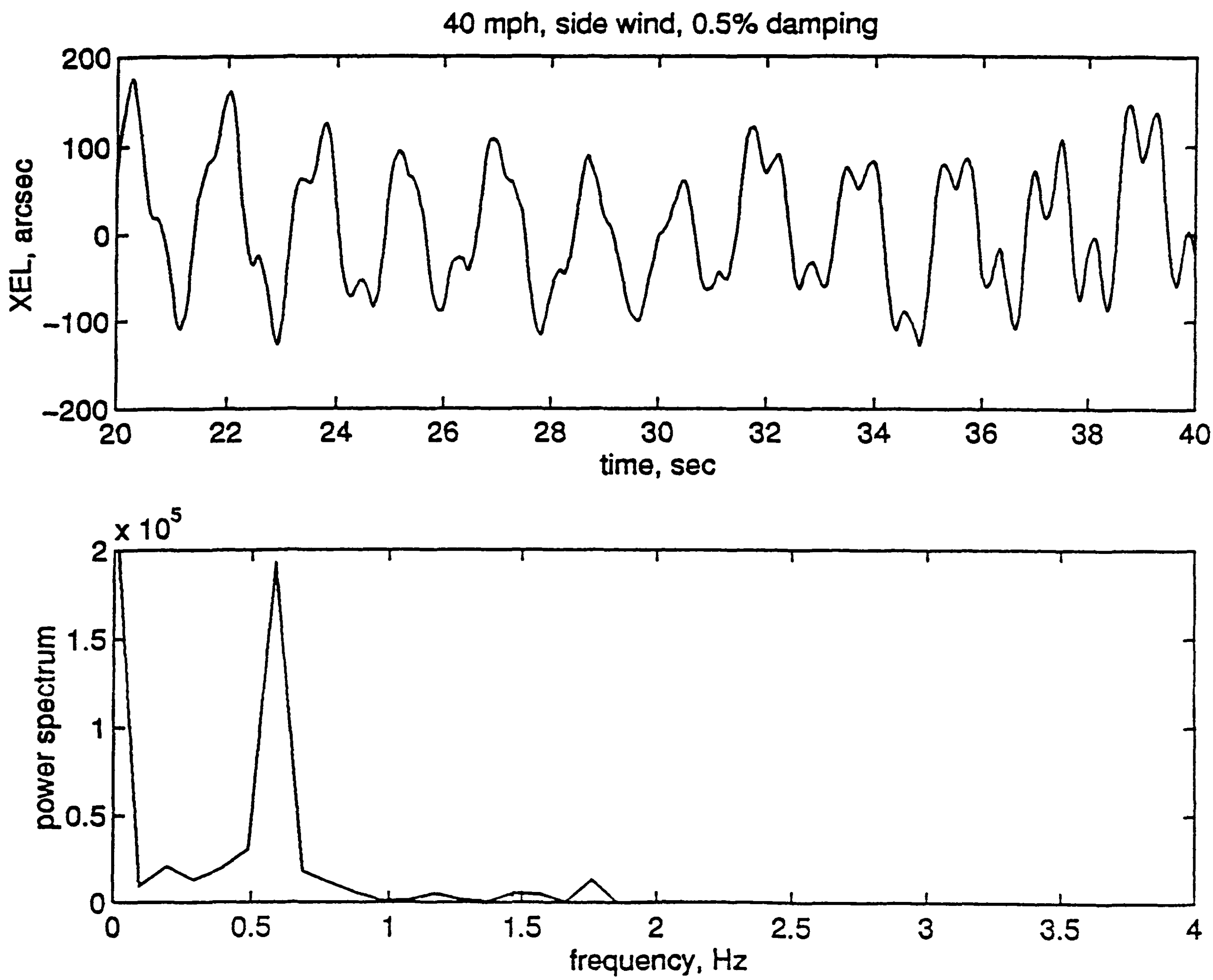

Fig.16c,d Detail of the simulations for the 40 mph side wind gusts, (c) cross-elevation pointing error, (d) spectrum of the cross-elevation pointing error.

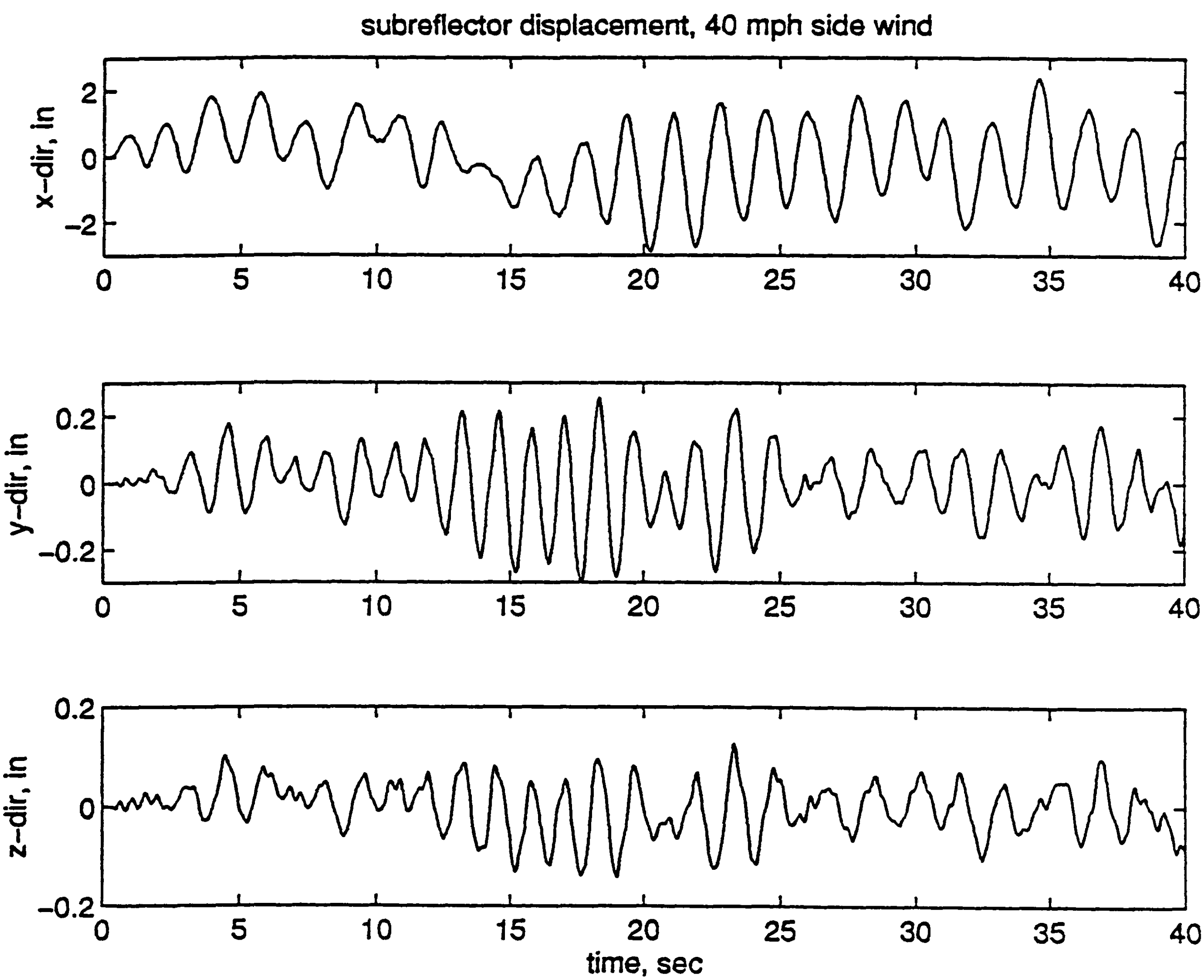

Fig. 17. **Subreflector displacement for the 40 mph side wind, (a) *x*-direction, (b) *y*-direction, and (c) *z*-direction.**

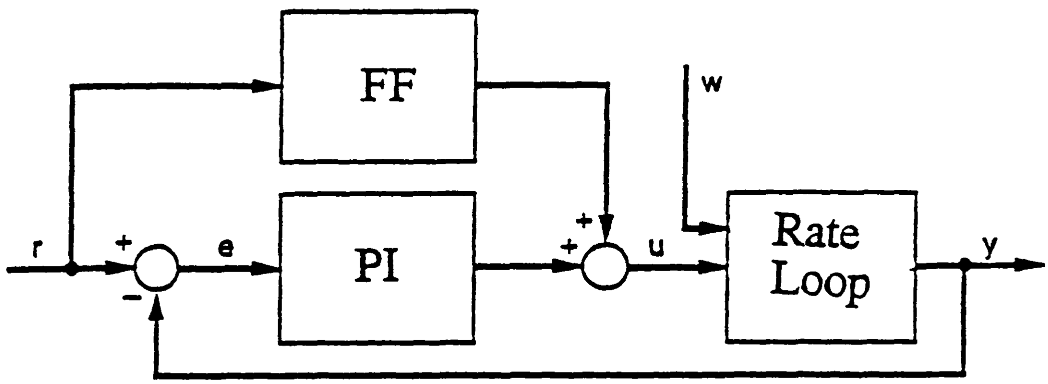

Fig.18. Position loop with the rate feed-forward.

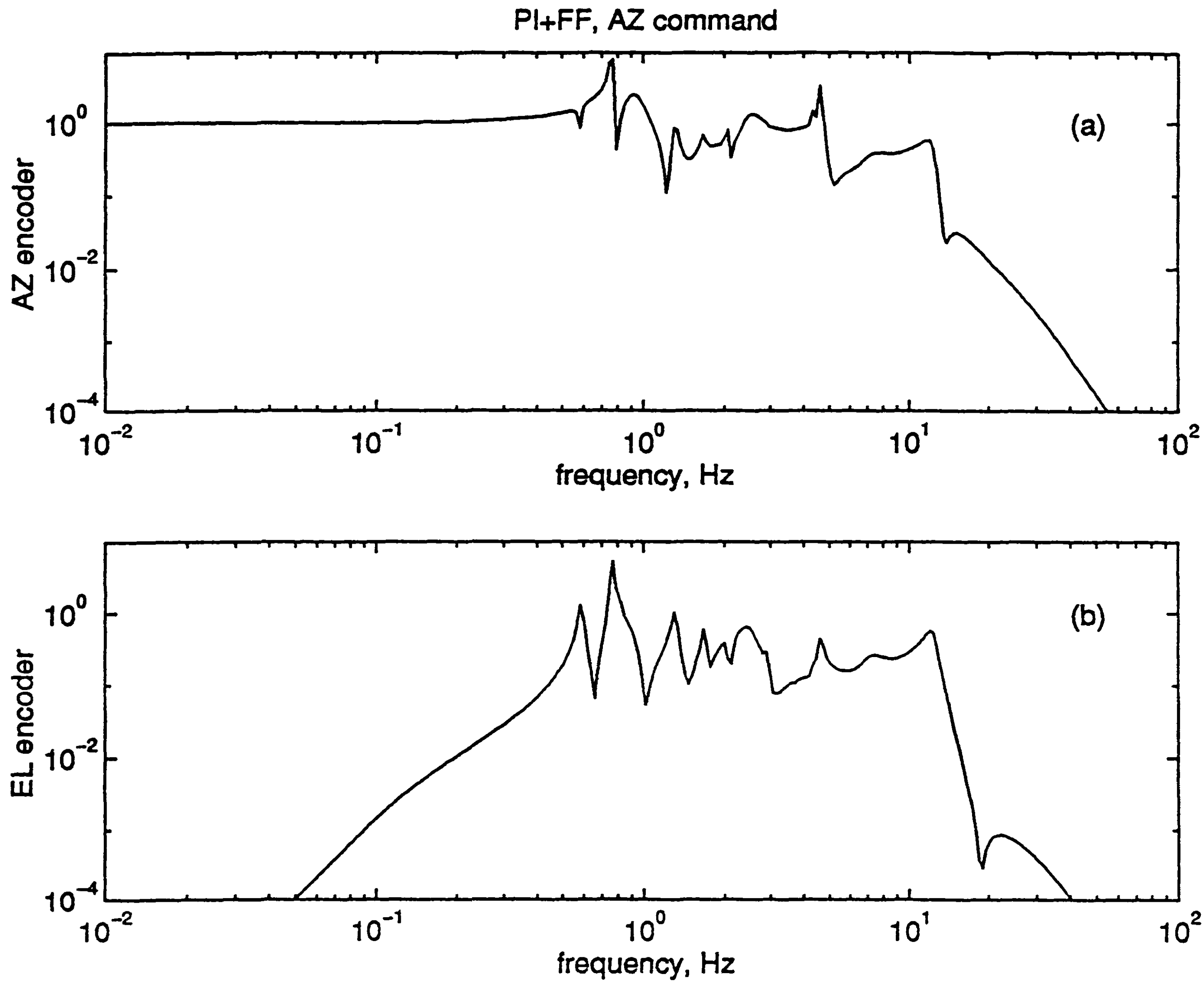

Fig.19. Magnitude of the transfer functions for the PI+FF controller, from the azimuth command to (a) azimuth encoder, (b) elevation encoder.

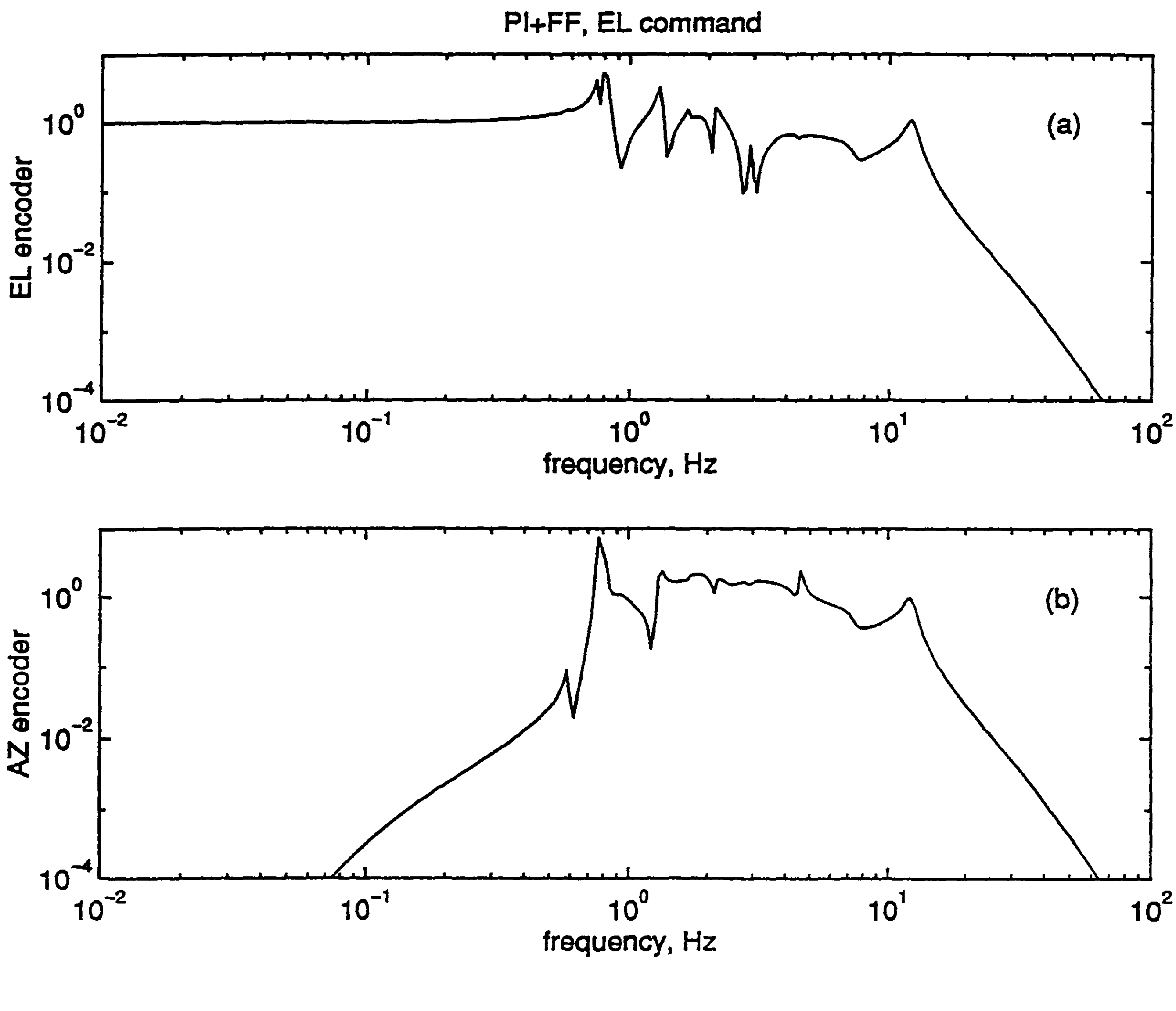

Fig.20. Magnitude of the transfer functions for the PI+FF controller, from the elevation command to (a) elevation encoder, (b) azimuth encoder.

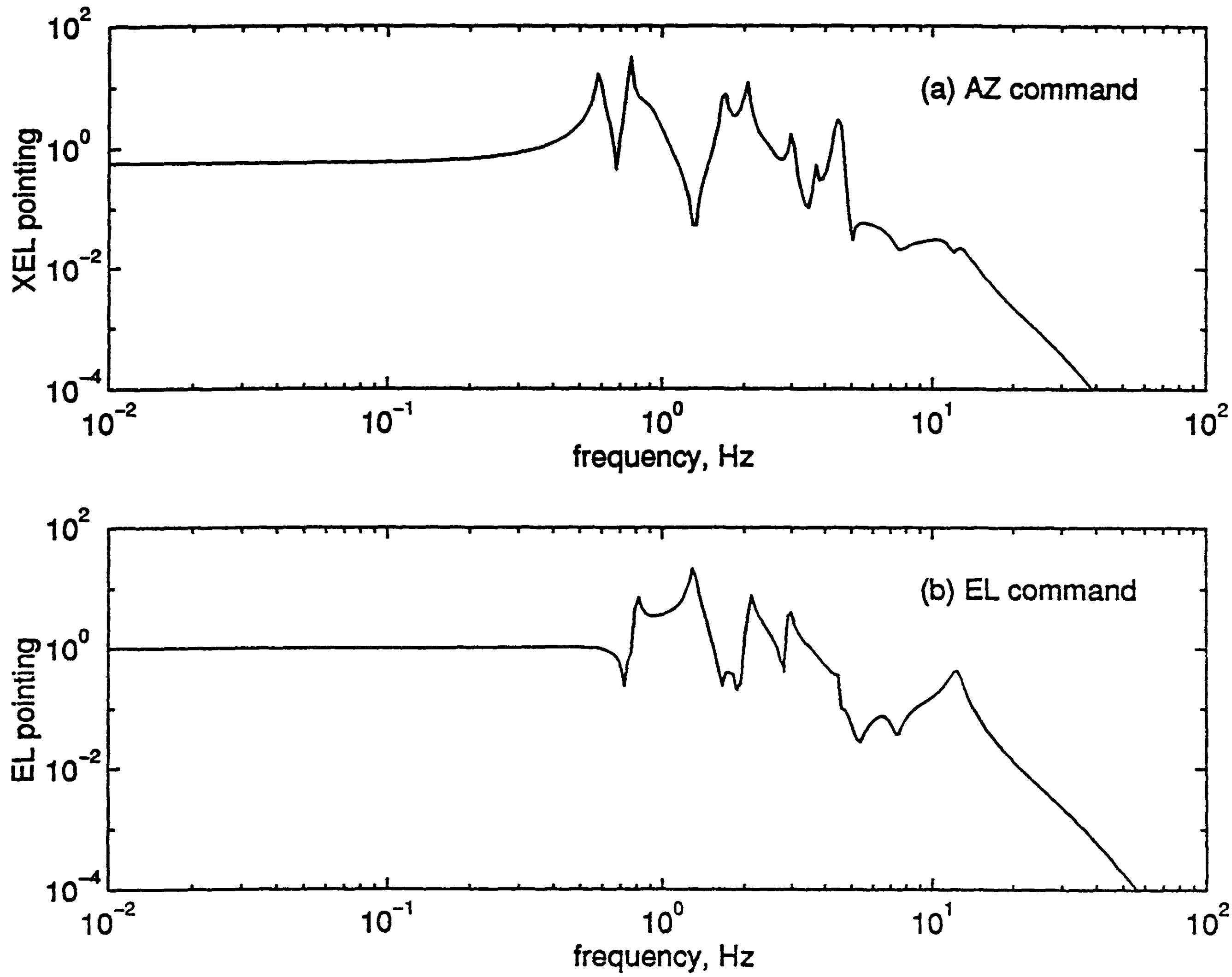

Fig.21. Magnitude of the transfer functions for the PI+FF controller, (a) from the azimuth command to cross-elevation pointing, (b) from the elevation command to elevation pointing.

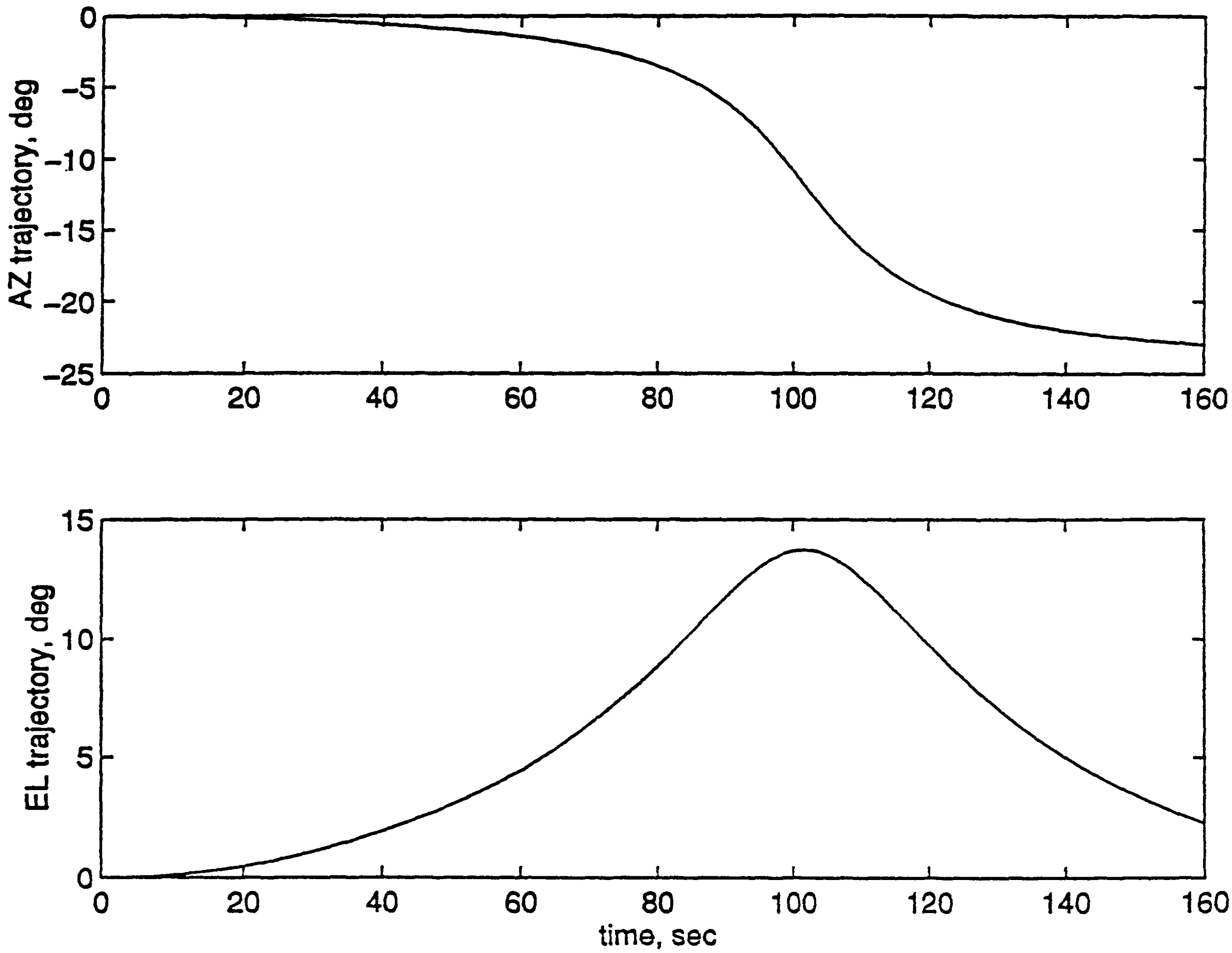

Fig.22. Trajectories: (a) in azimuth, (b) in elevation.

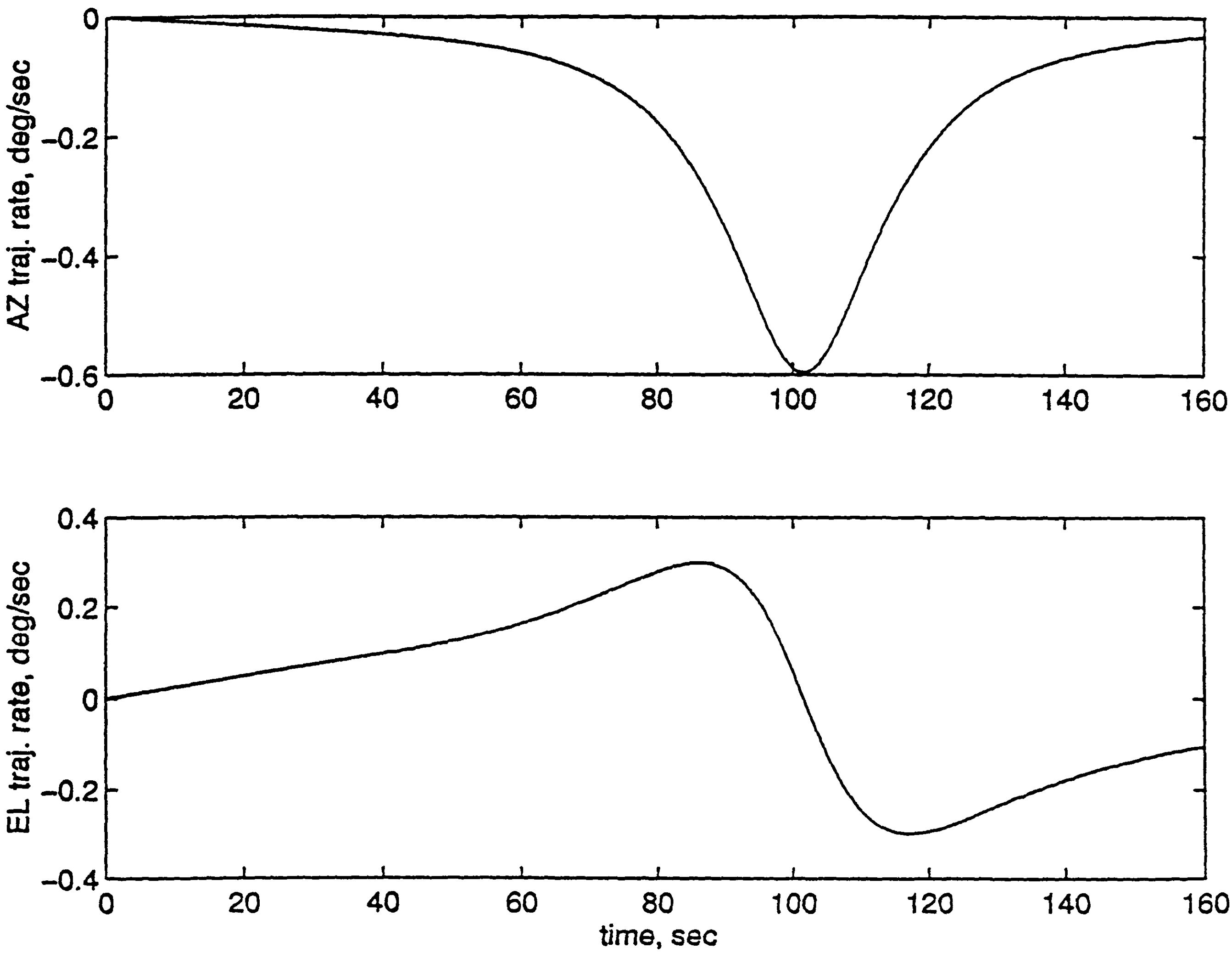

Fig.23. Trajectory rates: (a) in azimuth, (b) in elevation.

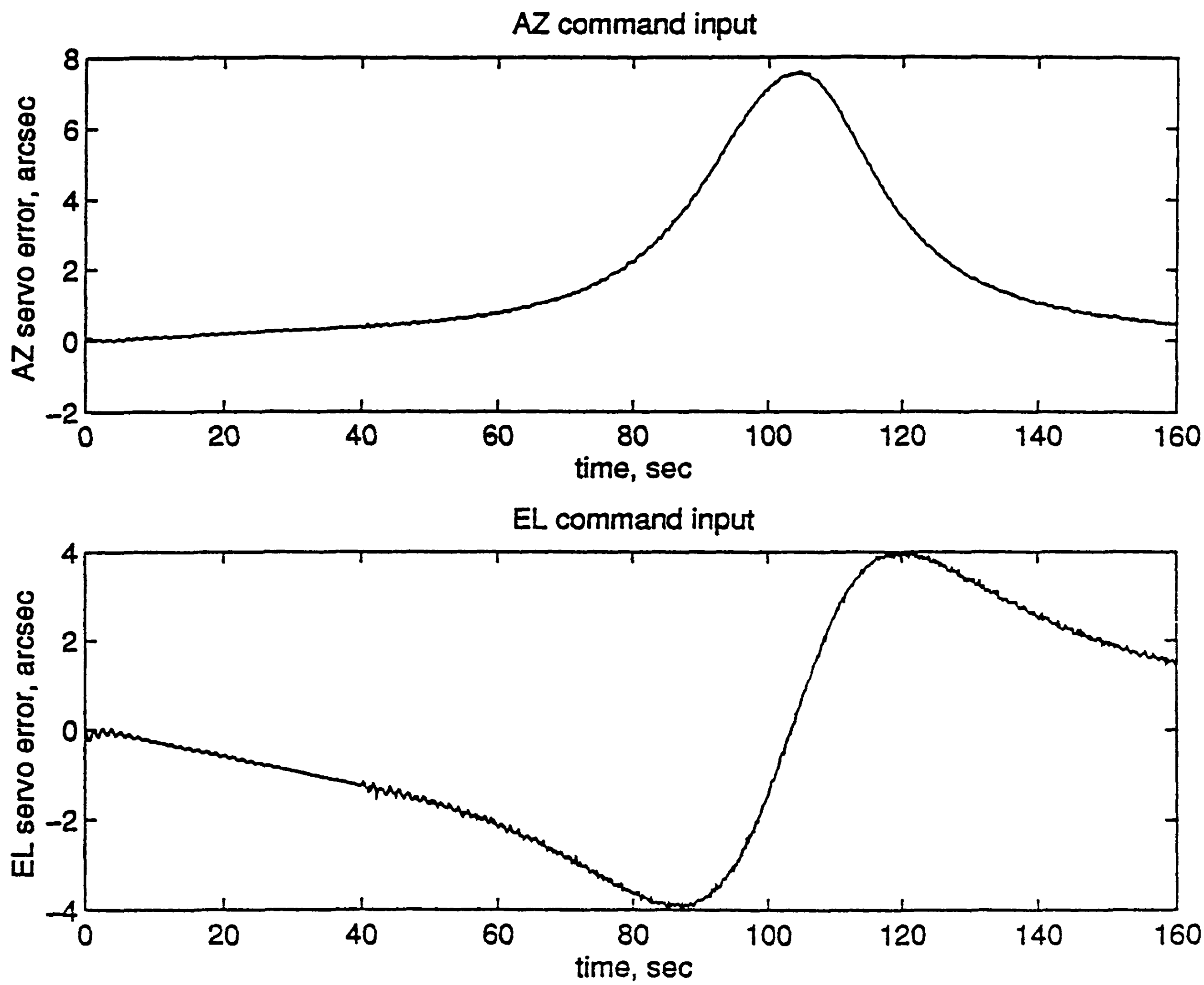

Fig.24. (a) azimuth servo error, for the azimuth command input, (b) elevation servo error, for the elevation command input.

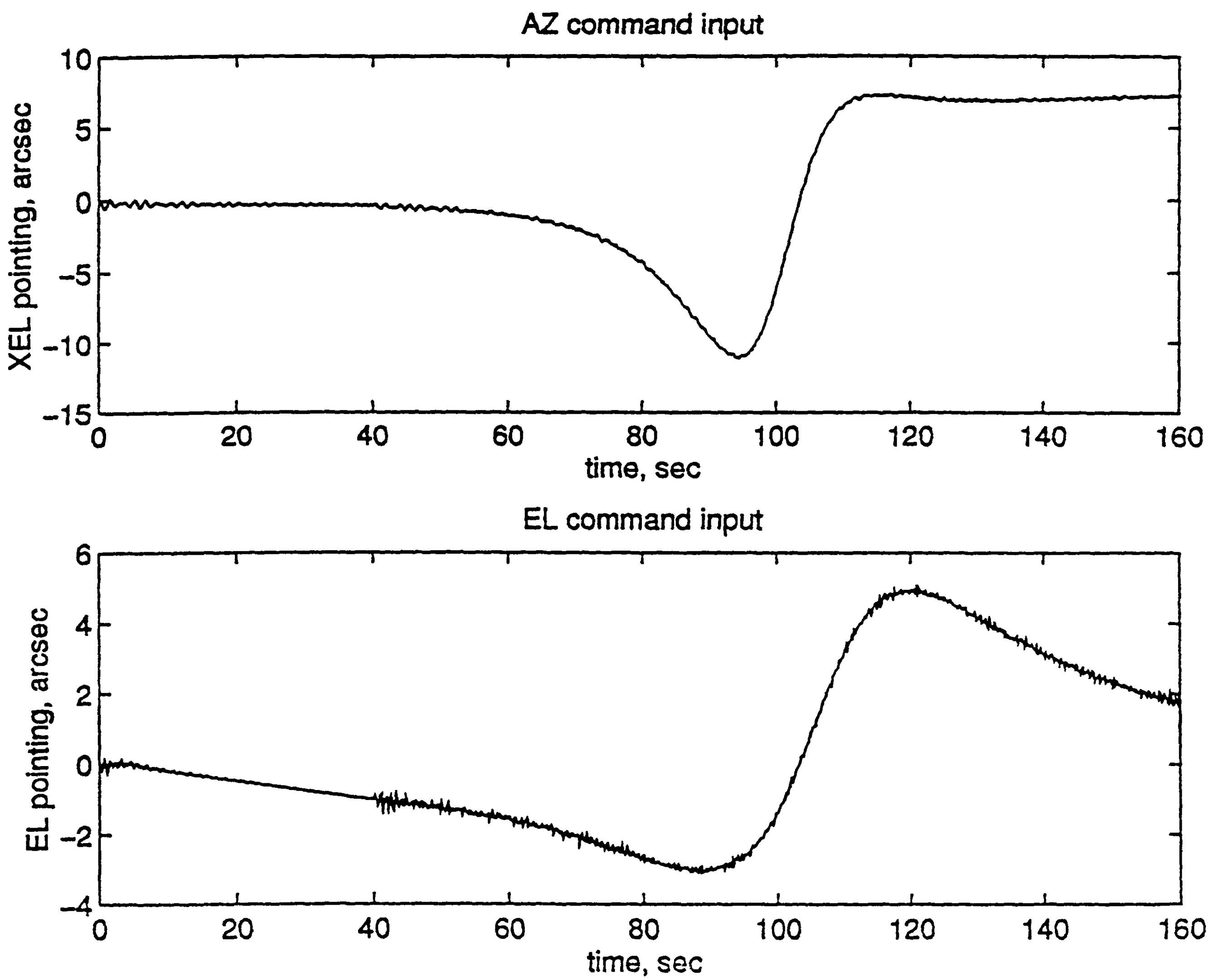

Fig.25. (a) Cross-elevation pointing error, for the azimuth command input,
(b) elevation pointing error, for the elevation command input.

1% damping
PI+feedforward controller with pre-processor
Antenna orientation 60 deg in EL
Acceleration limit 0.2 deg/sec^2
Rate limit 0.67 in AZ, 0.33 in EL

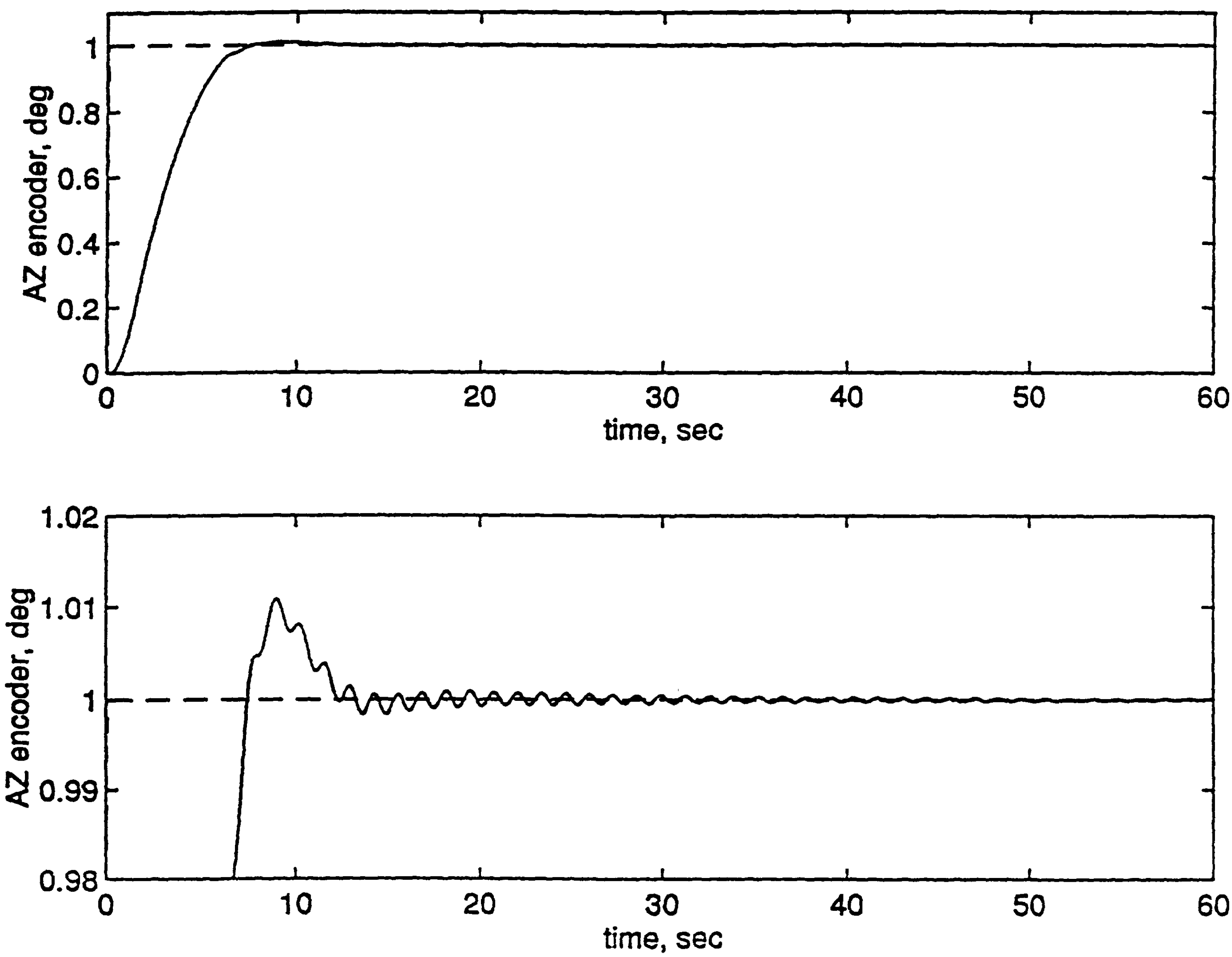

Fig.26. Antenna azimuth encoder response to 1 deg step in azimuth (a) full figure, (b) zoomed figure.

1% damping
PI+feedforward controller with pre-processor
Antenna orientation 60 deg in EL
Acceleration limit 0.2 deg/sec²
Rate limit 0.67 in AZ, 0.33 in EL

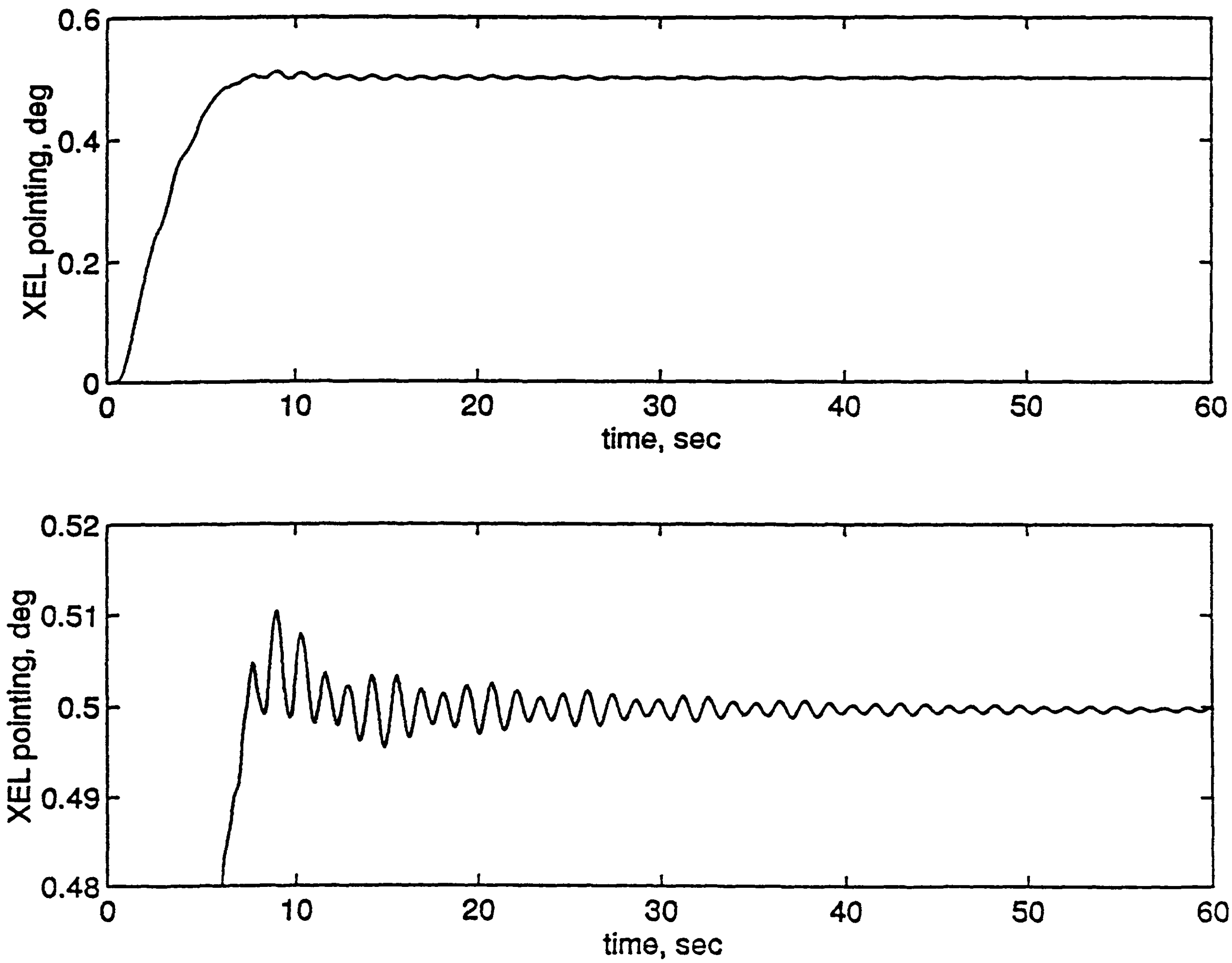

Fig.27. Antenna cross-elevation beam response to 1 deg step in azimuth (a) full figure, (b) zoomed figure.

1% damping
PI+feedforward controller with pre-processor
Antenna orientation 60 deg in EL
Acceleration limit 0.2 deg/sec²
Rate limit 0.67 in AZ, 0.33 in EL

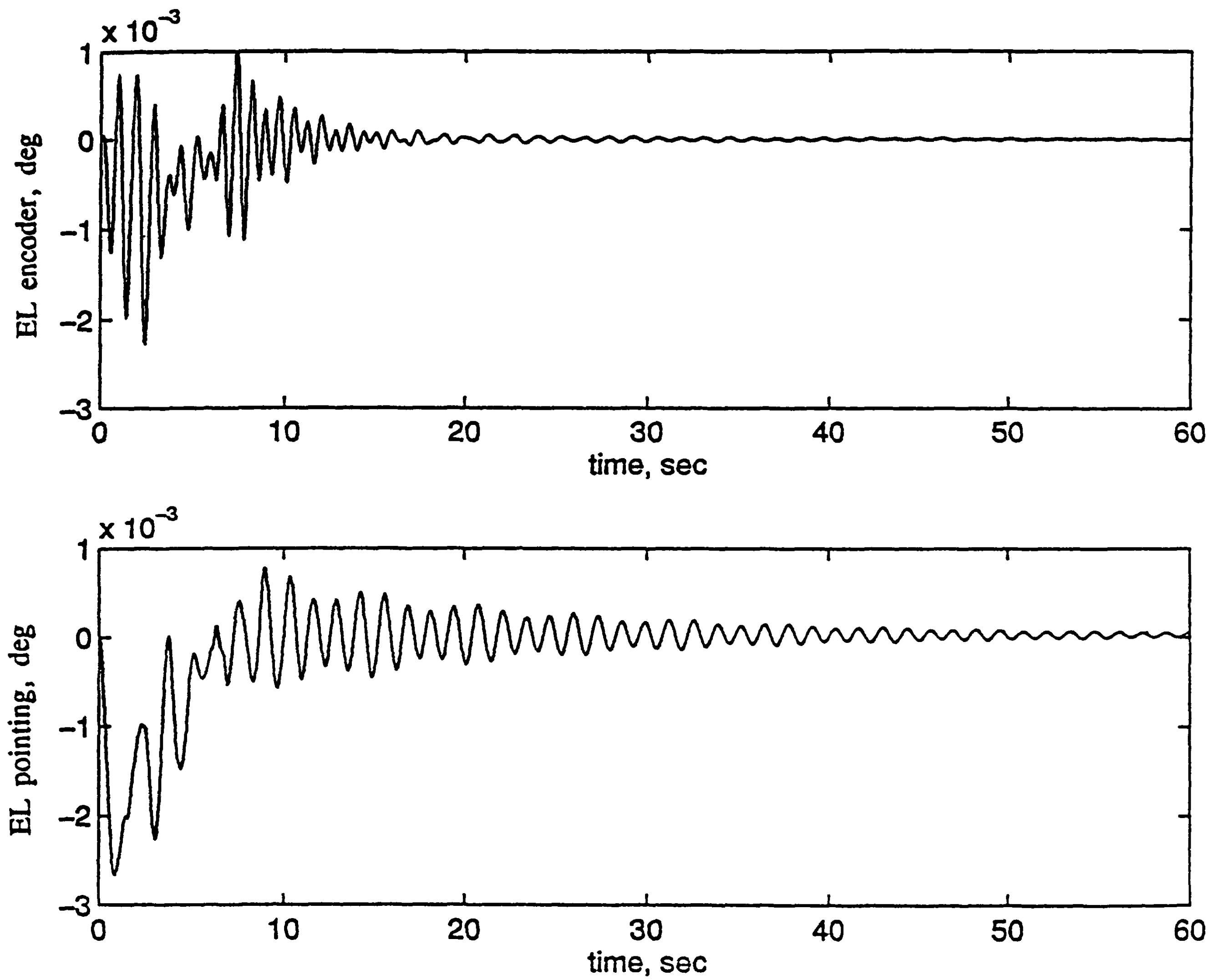

Fig.28. **Antenna responses to 1 deg step in azimuth: (a) elevation encoder and (b) elevation beam.**

1% damping
PI+feedforward controller with pre-processor
Antenna orientation 60 deg in EL
Acceleration limit 0.2 deg/sec²
Rate limit 0.67 in AZ, 0.33 in EL

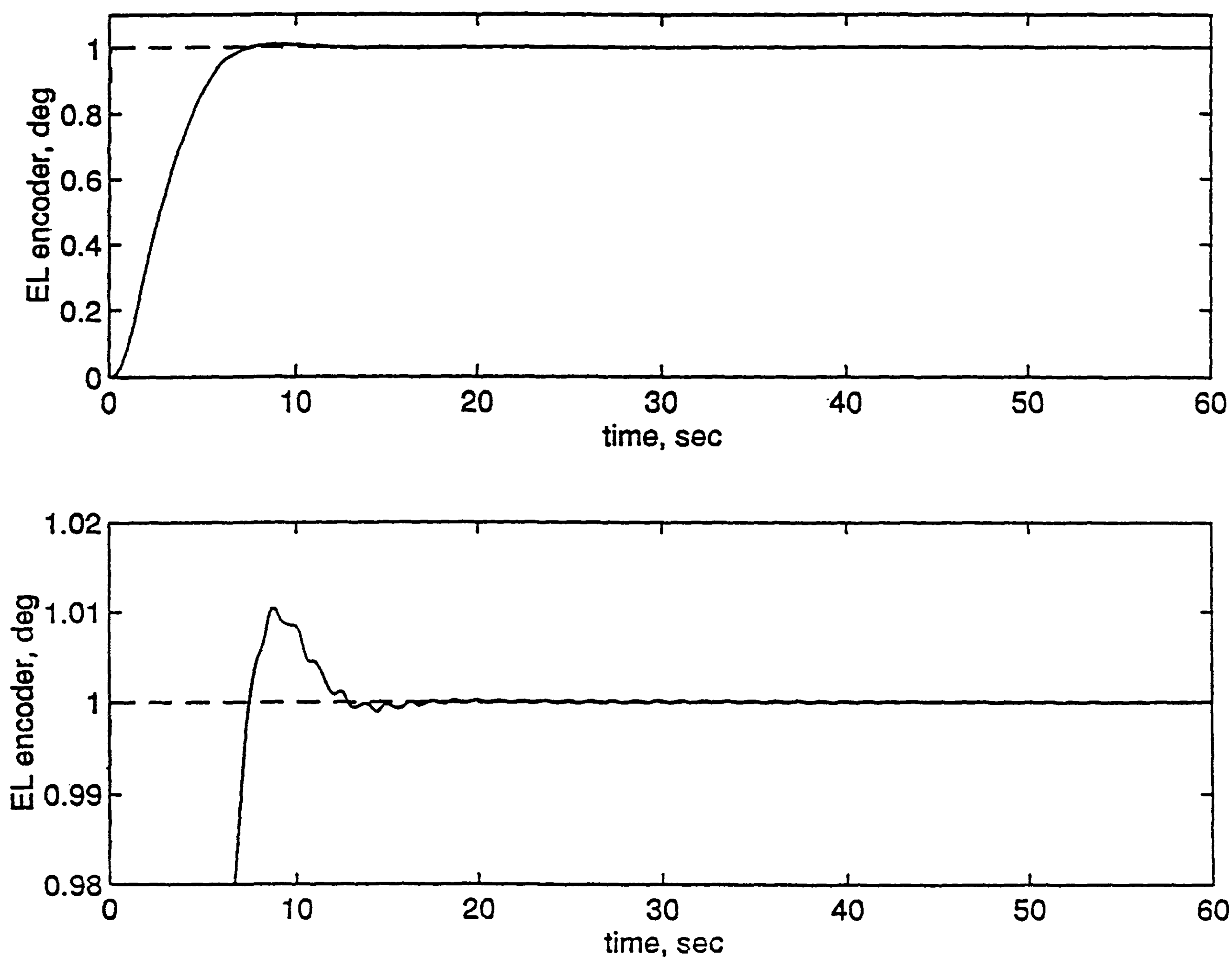

Fig.29. Antenna elevation encoder response to 1 deg step in elevation (a) full figure, (b) zoomed figure.

1% damping
PI+feedforward controller with pre-processor
Antenna orientation 60 deg in EL
Acceleration limit 0.2 deg/sec^2
Rate limit 0.67 in AZ, 0.33 in EL

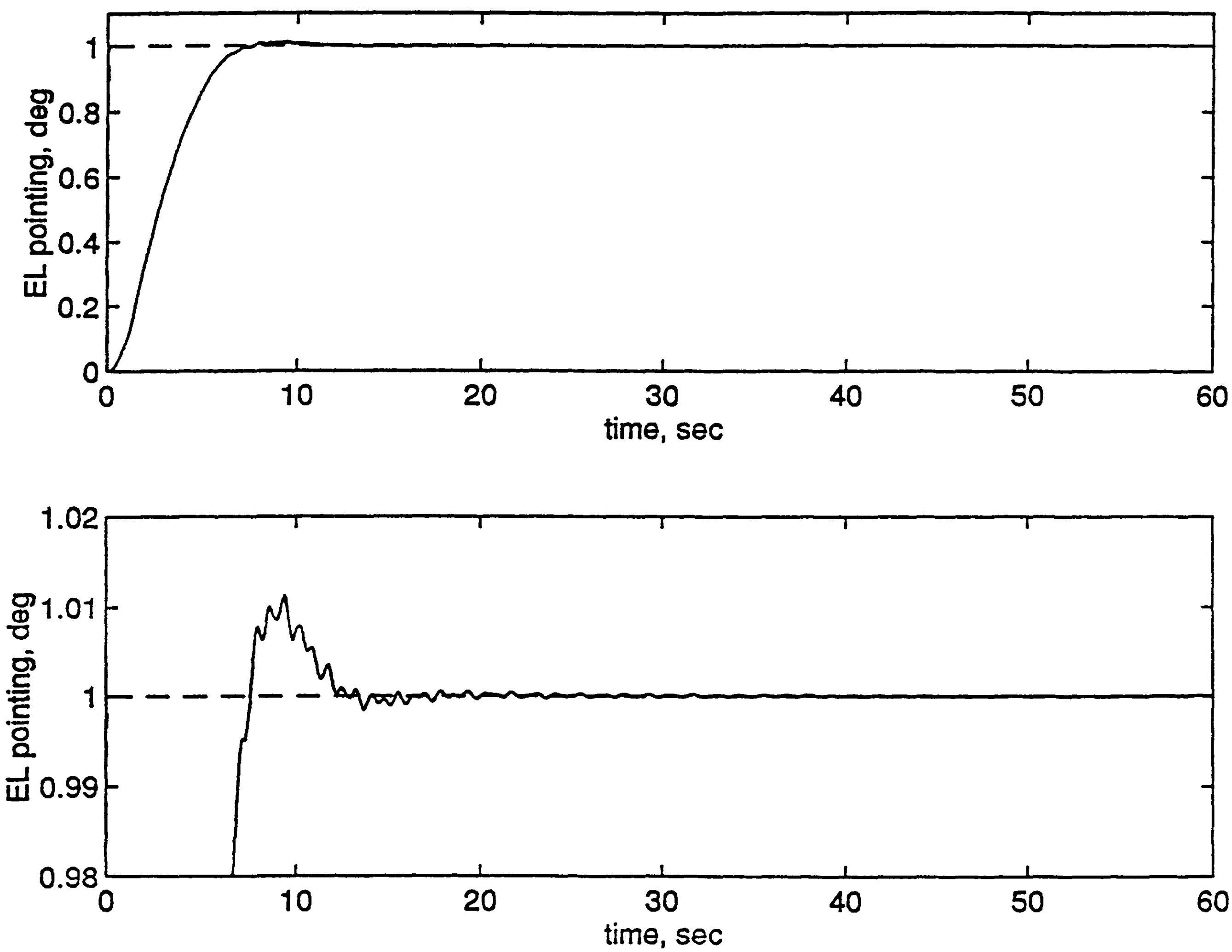

Fig.30. Antenna elevation pointing response to 1 deg step in elevation (a) full figure, (b) zoomed figure.

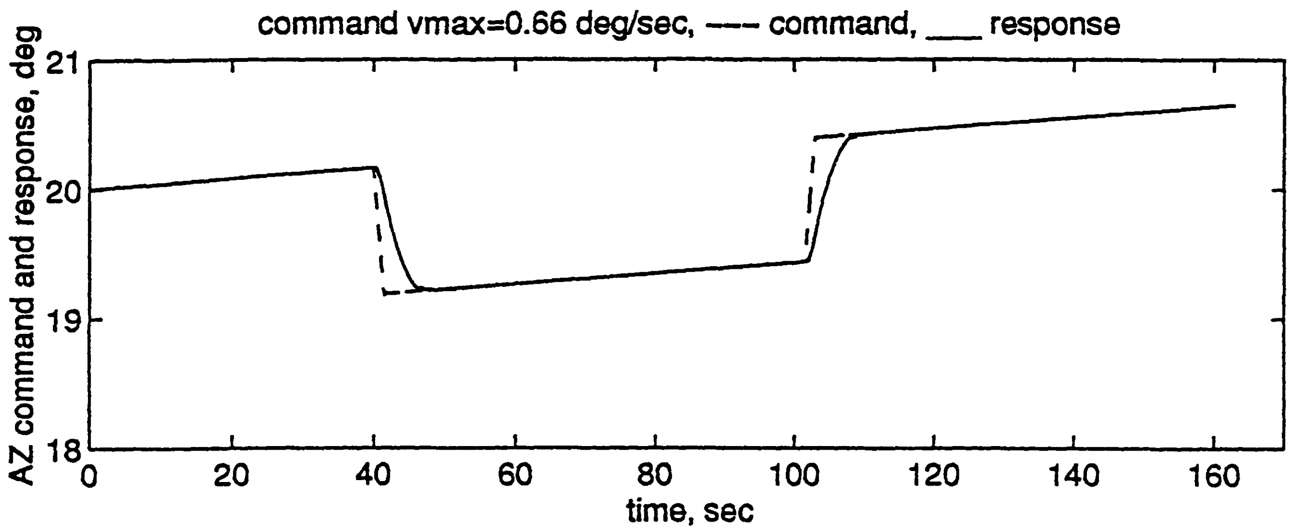

Fig.31. The response at the azimuth encoder (solid line) to the azimuth command (dashed line). The command rate is sidereal (0.0042 deg/sec) with rapid changes at max. rate (0.67 deg/sec). PCD preprocessor was included in the simulations.

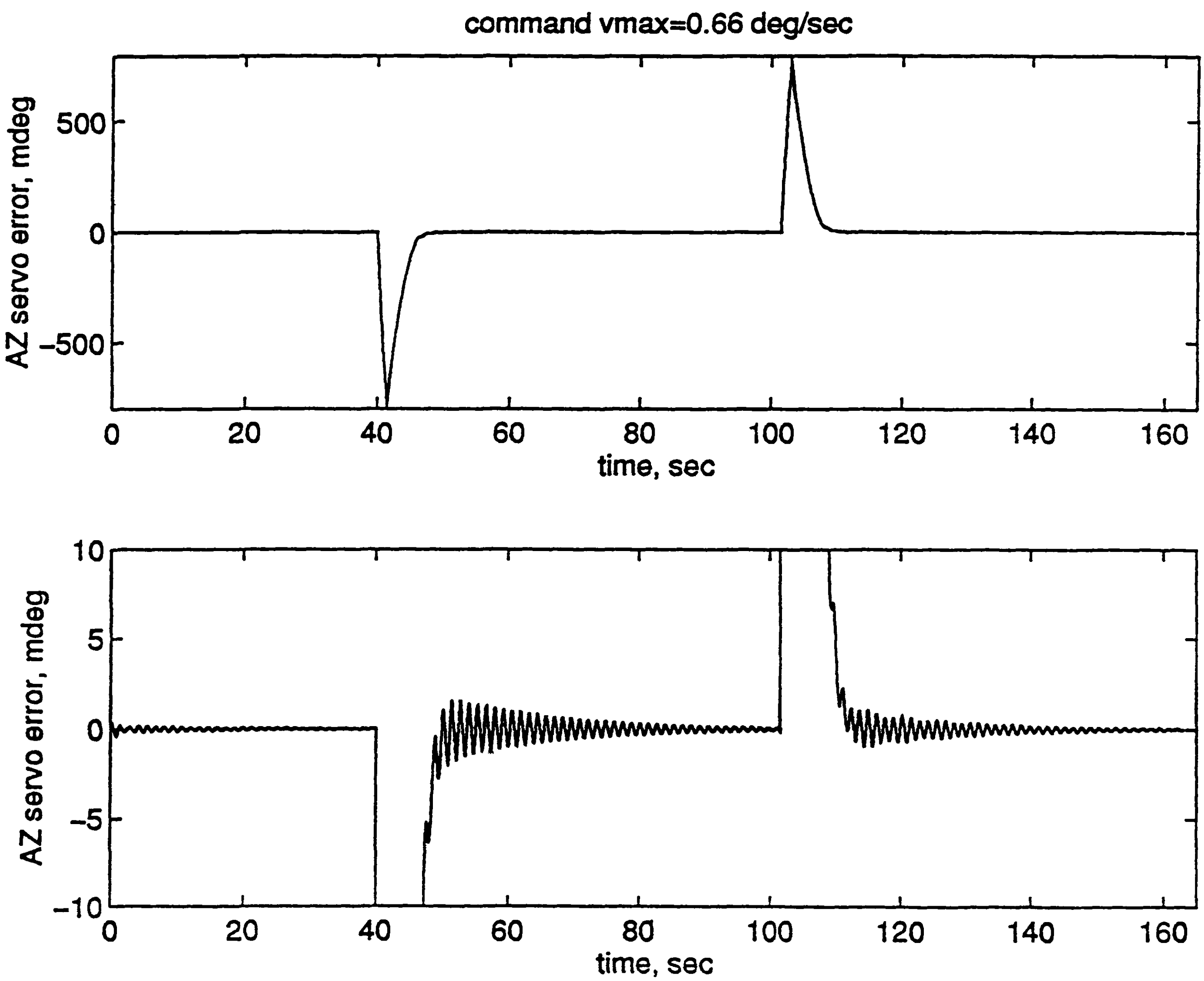

Fig.32. Azimuth encoder error for the azimuth command as in Fig.31, (a) full figure, (b) zoomed figure.

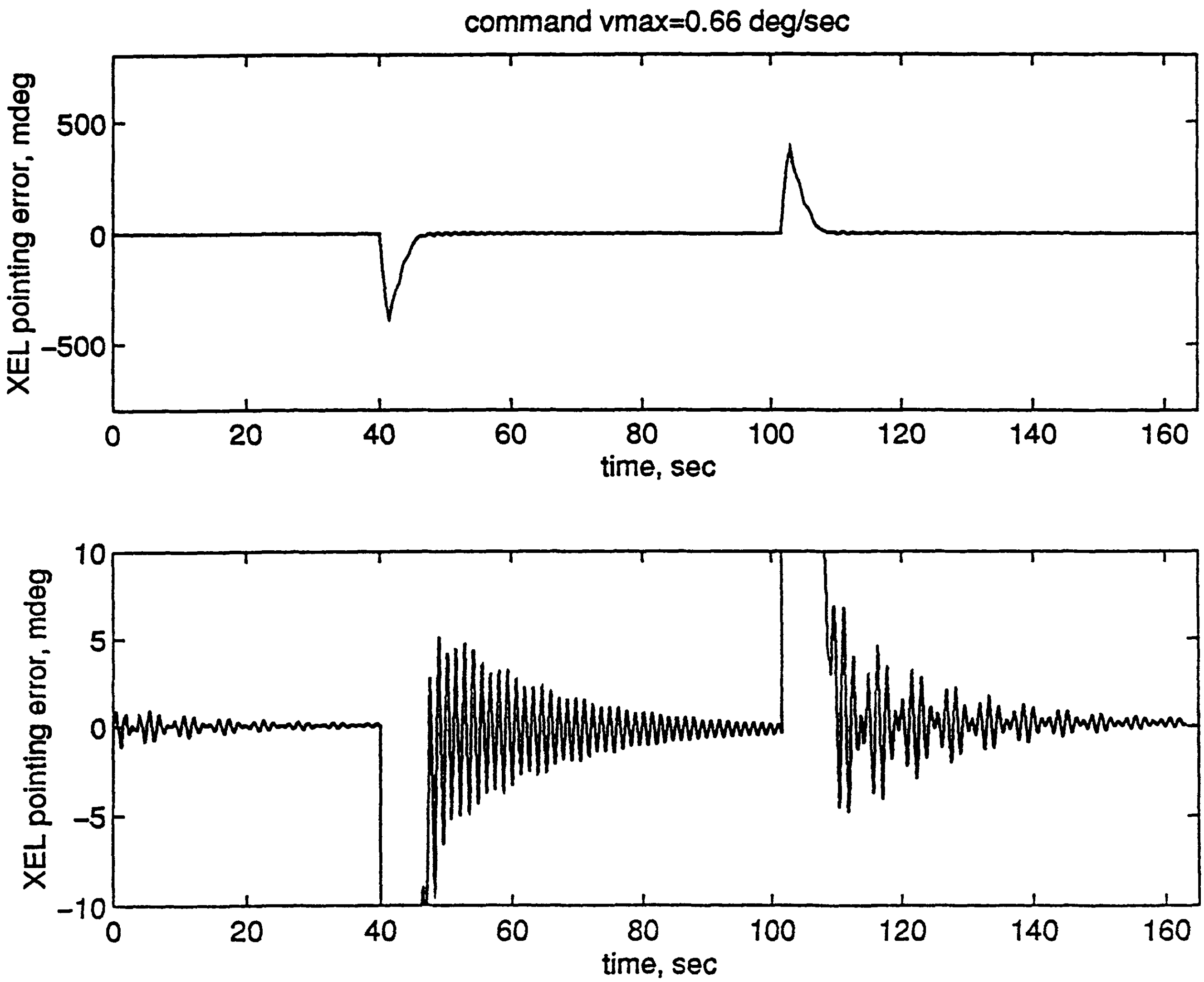

Fig.33. The cross-elevation beam error for the azimuth command as in Fig.31, (a) full figure, (b) zoomed figure.

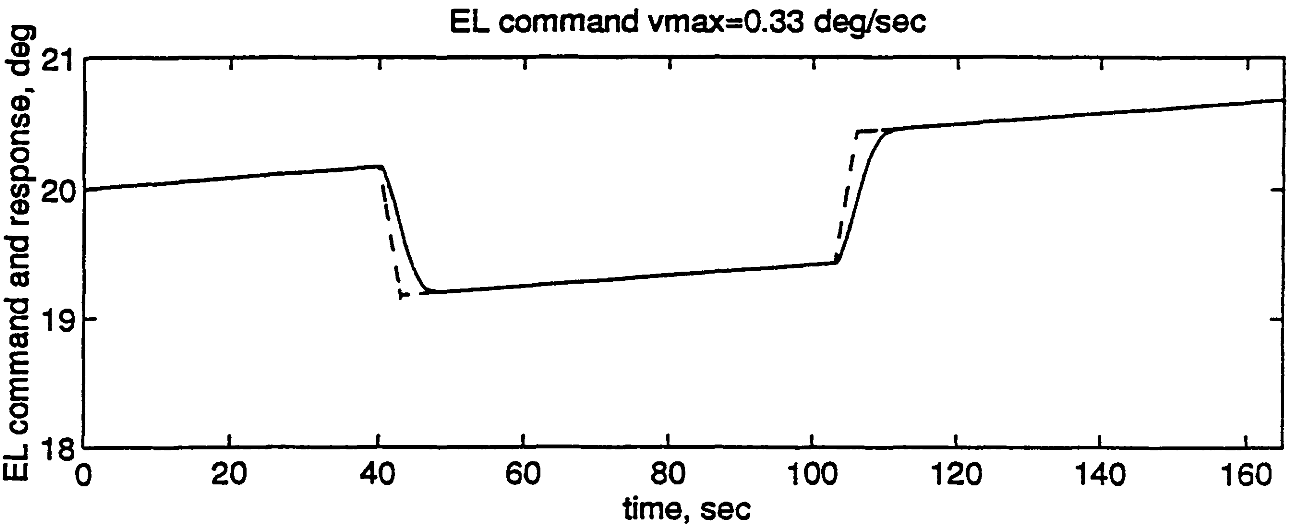

Fig.34. The response at the elevation encoder (solid line) to the elevation command (dashed line). The command rate is sidereal (0.0042 deg/sec) with rapid changes at max. rate (0.33 deg/sec). PCD preprocessor was included in the simulations.

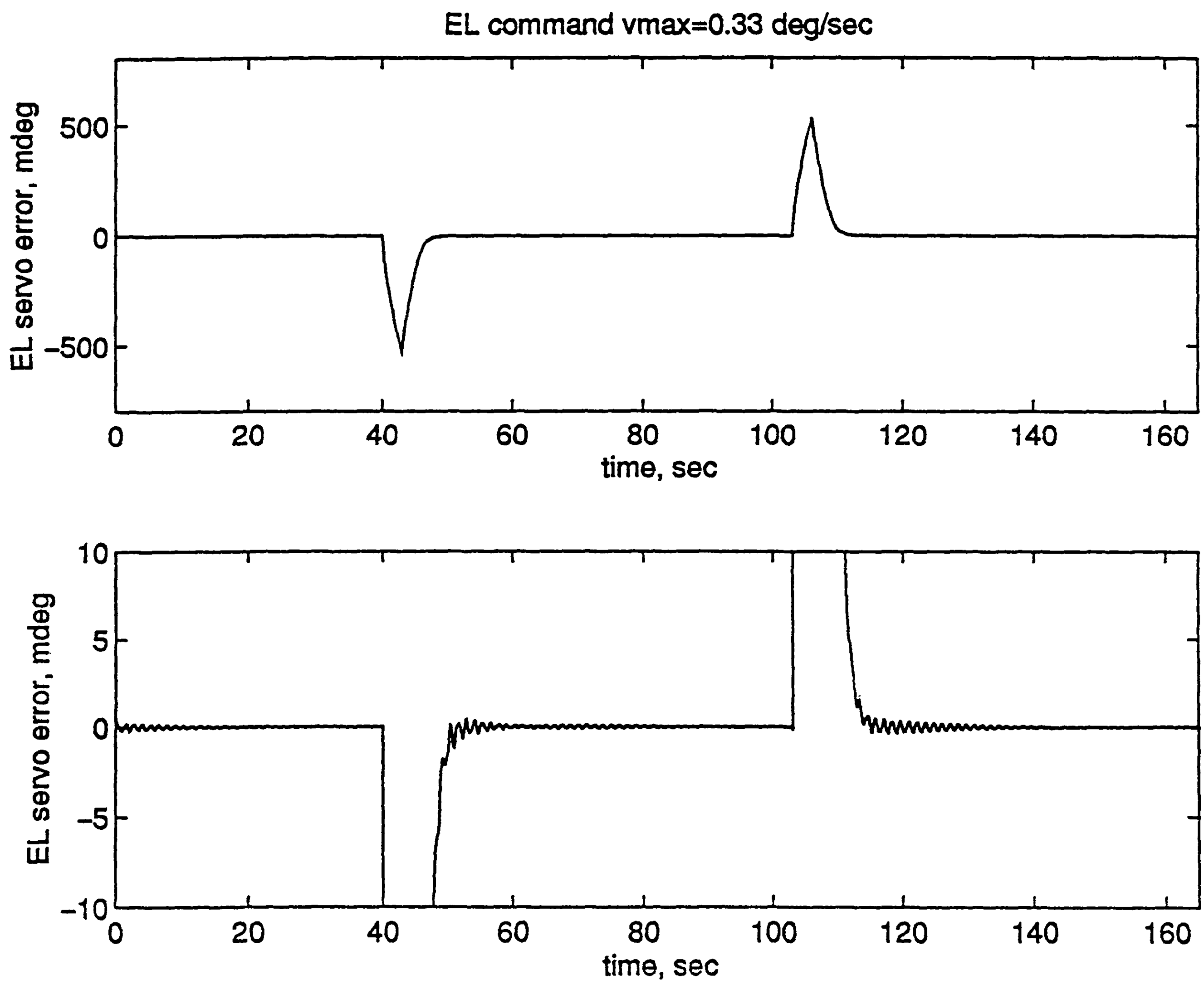

Fig.35. Elevation encoder error for the elevation command as in Fig.34, (a) full figure, (b) zoomed figure.

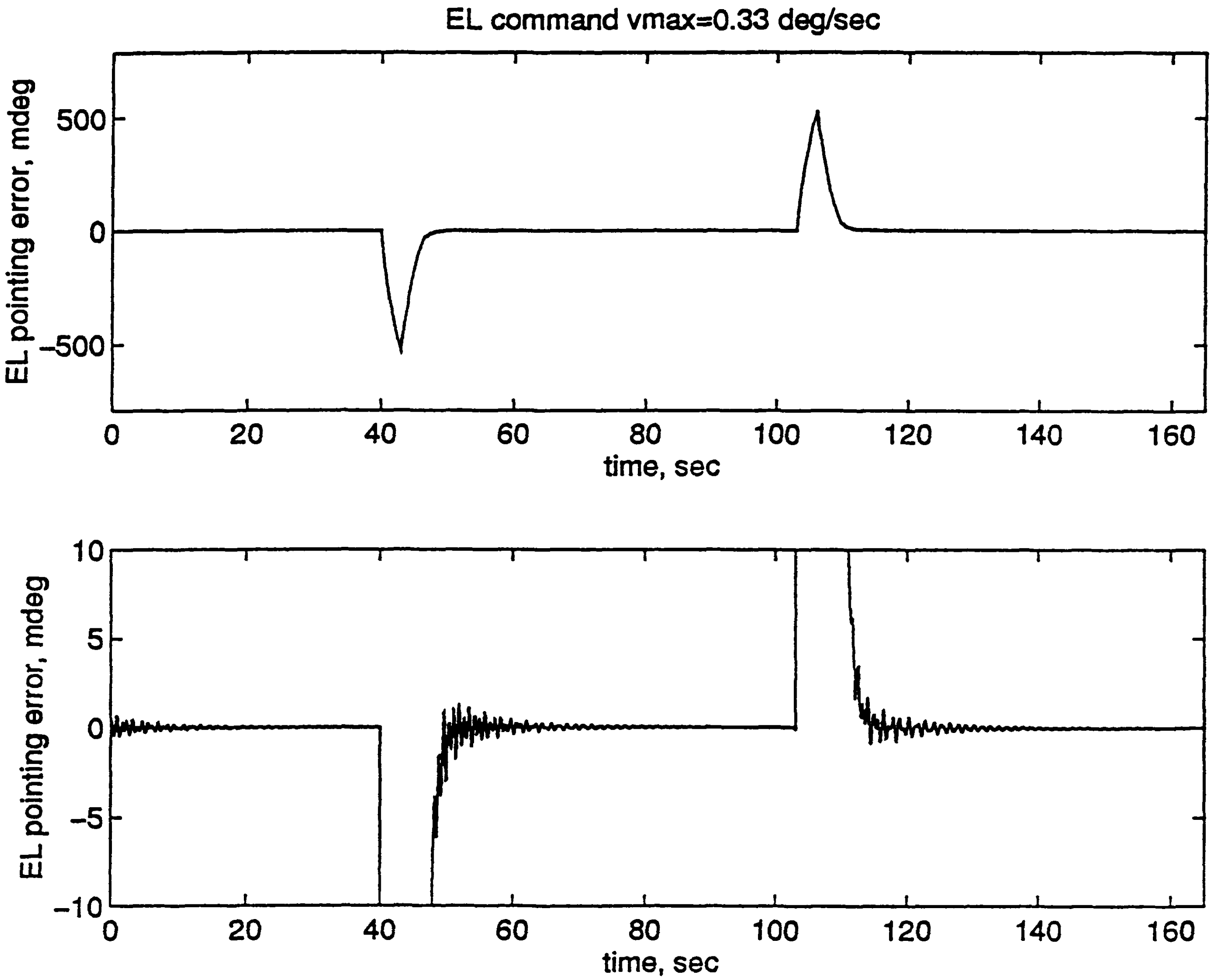

Fig.36. The elevation beam error for the elevation command as in Fig.34, (a) full figure, (b) zoomed figure.

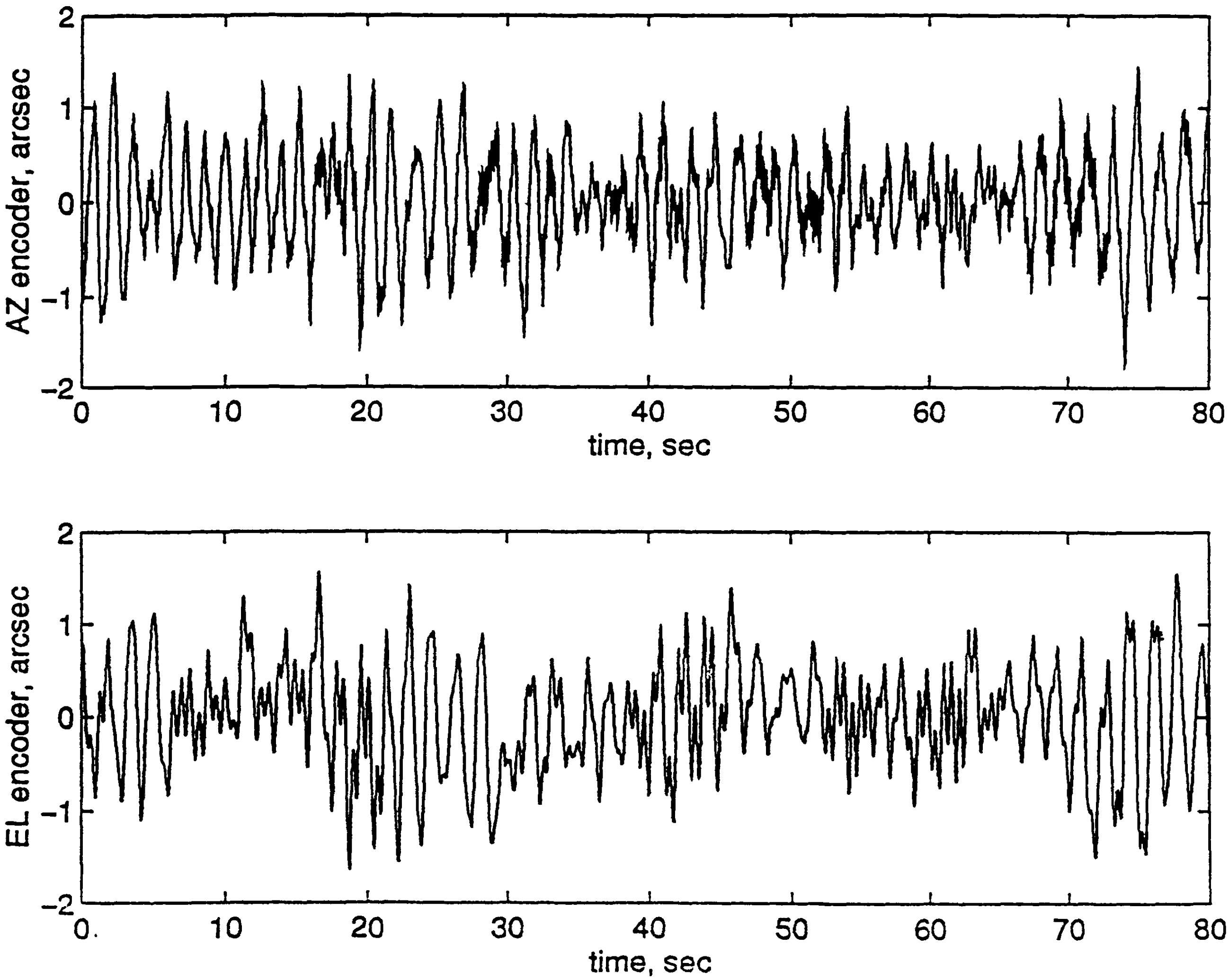

Fig.37. Antenna encoder responses to 7 m/s (15.6 mph) gusting (a) azimuth encoder, (b) elevation encoder. Wind direction along elevation axis, elevation position 60 deg. azimuth encoder rms=0.4 arcsec, elevation encoder rms=0.4 arcsec.

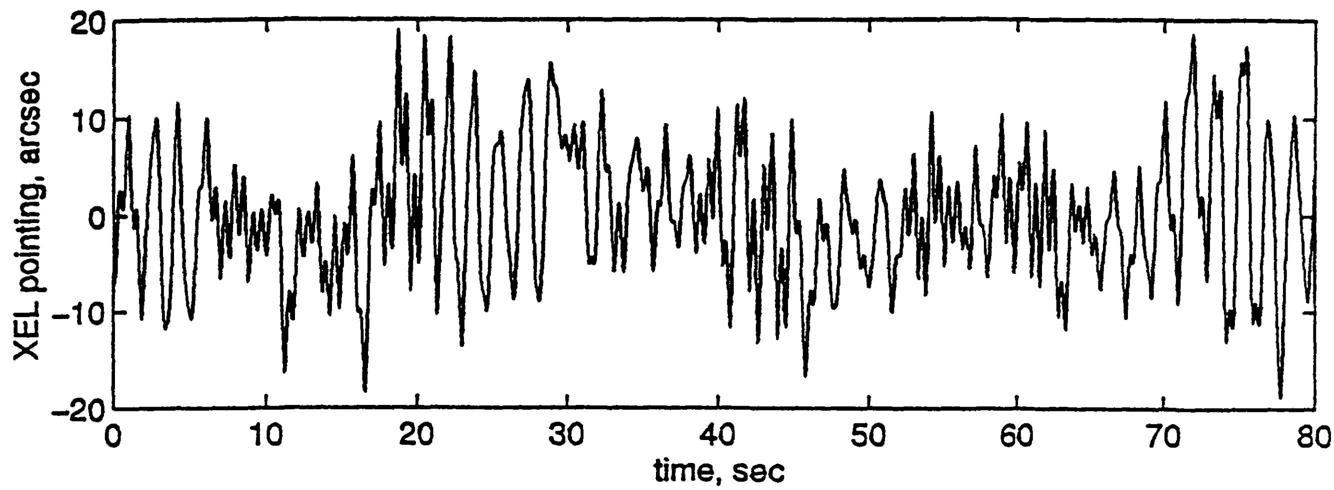

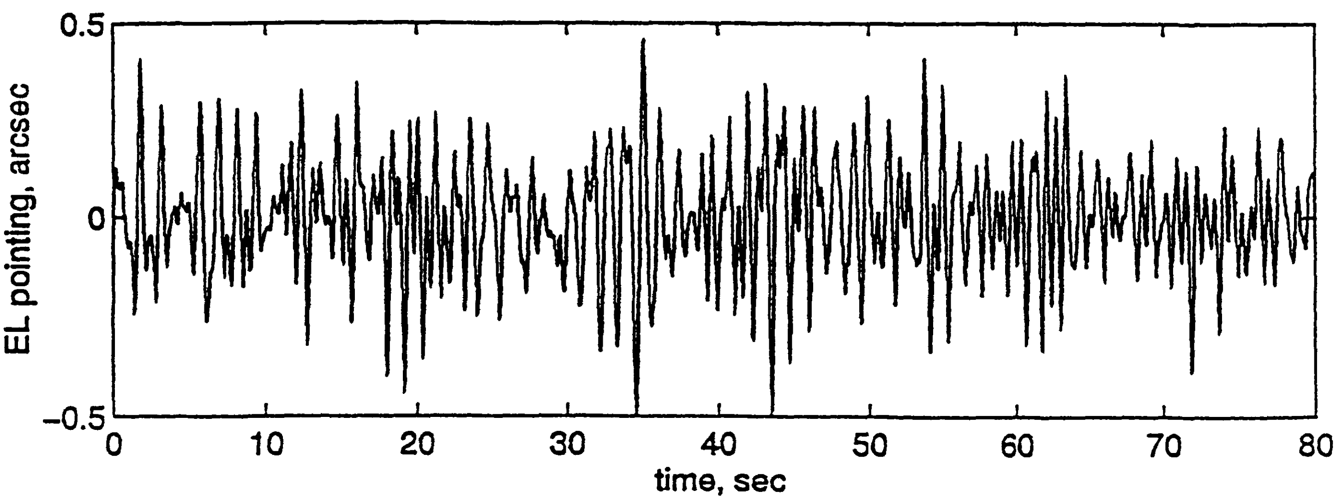

Fig.38. Antenna pointing responses to 7 m/s (15.6 mph) gusting, (a) cross-elevation beam pointing, (b) elevation beam pointing. Wind direction along elevation axis, elevation position 60 deg. cross-elevation pointing=7.9 arcsec, elevation pointing=0.16 arcsec.

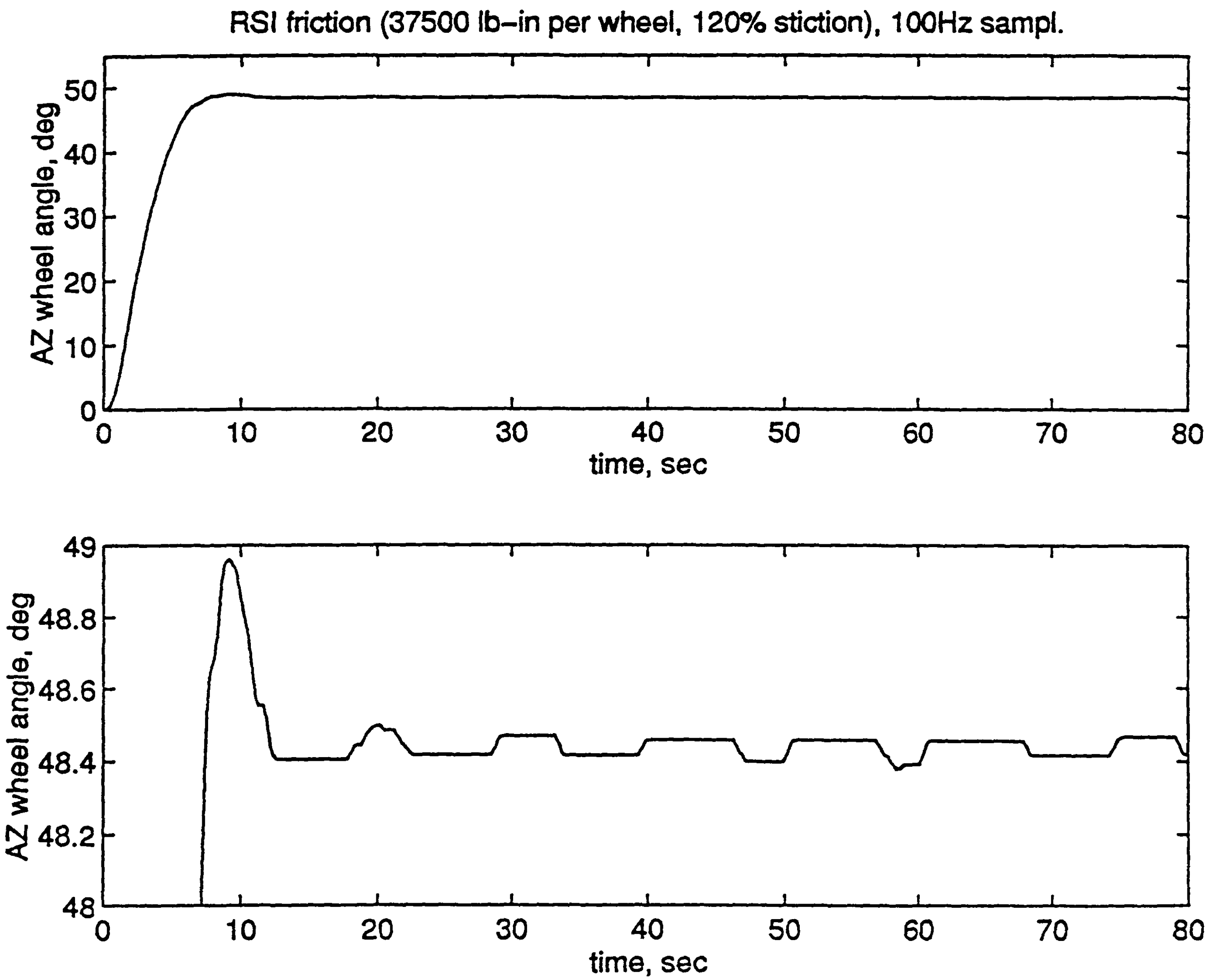

Fig.39. The azimuth wheel rotation, for 1 deg step command in azimuth, with the preprocessor (a) full figure, (b) zoomed figure.

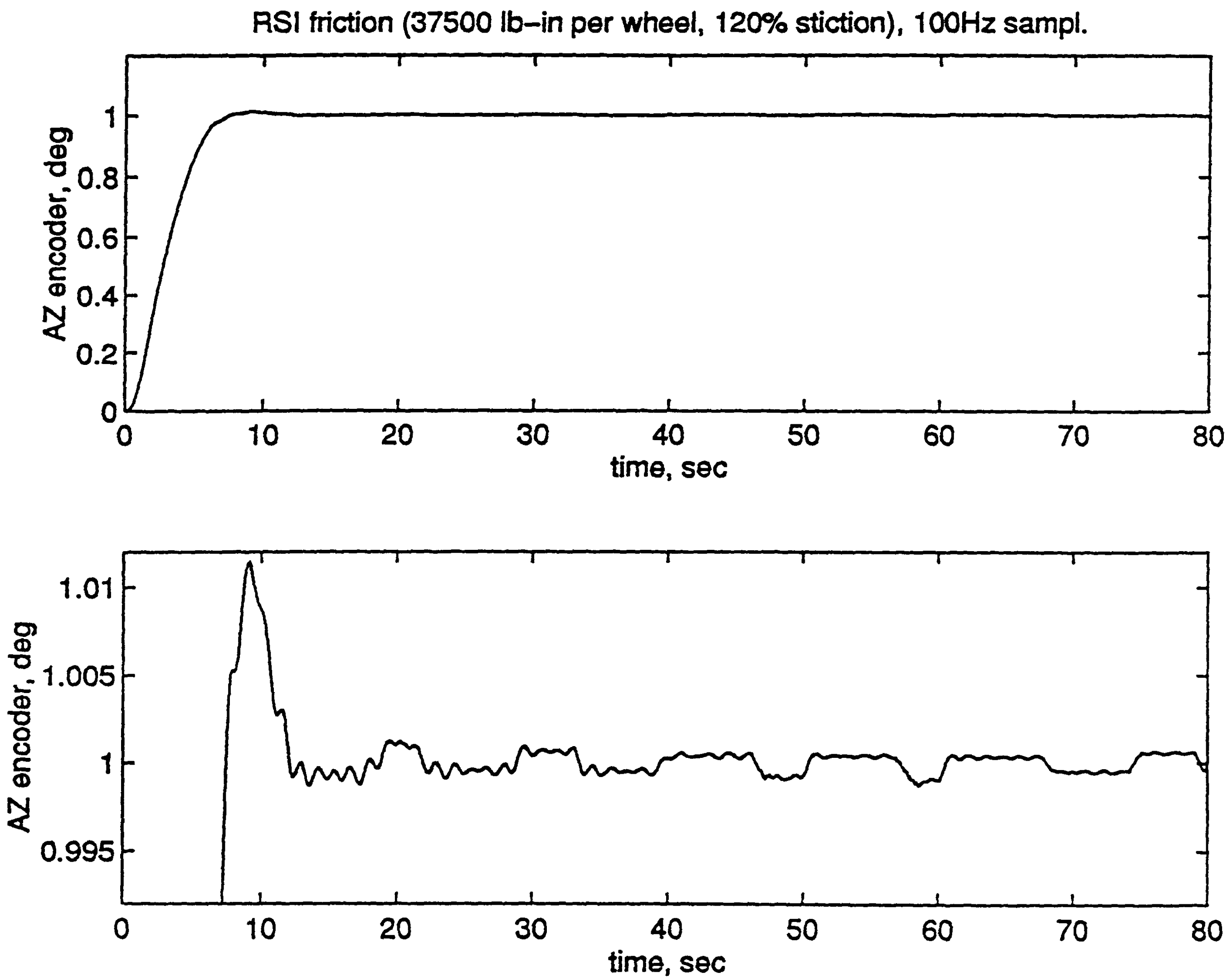

Fig.40. The azimuth encoder reading for 1 deg step command in azimuth, with the preprocessor (a) full figure, (b) zoomed figure.

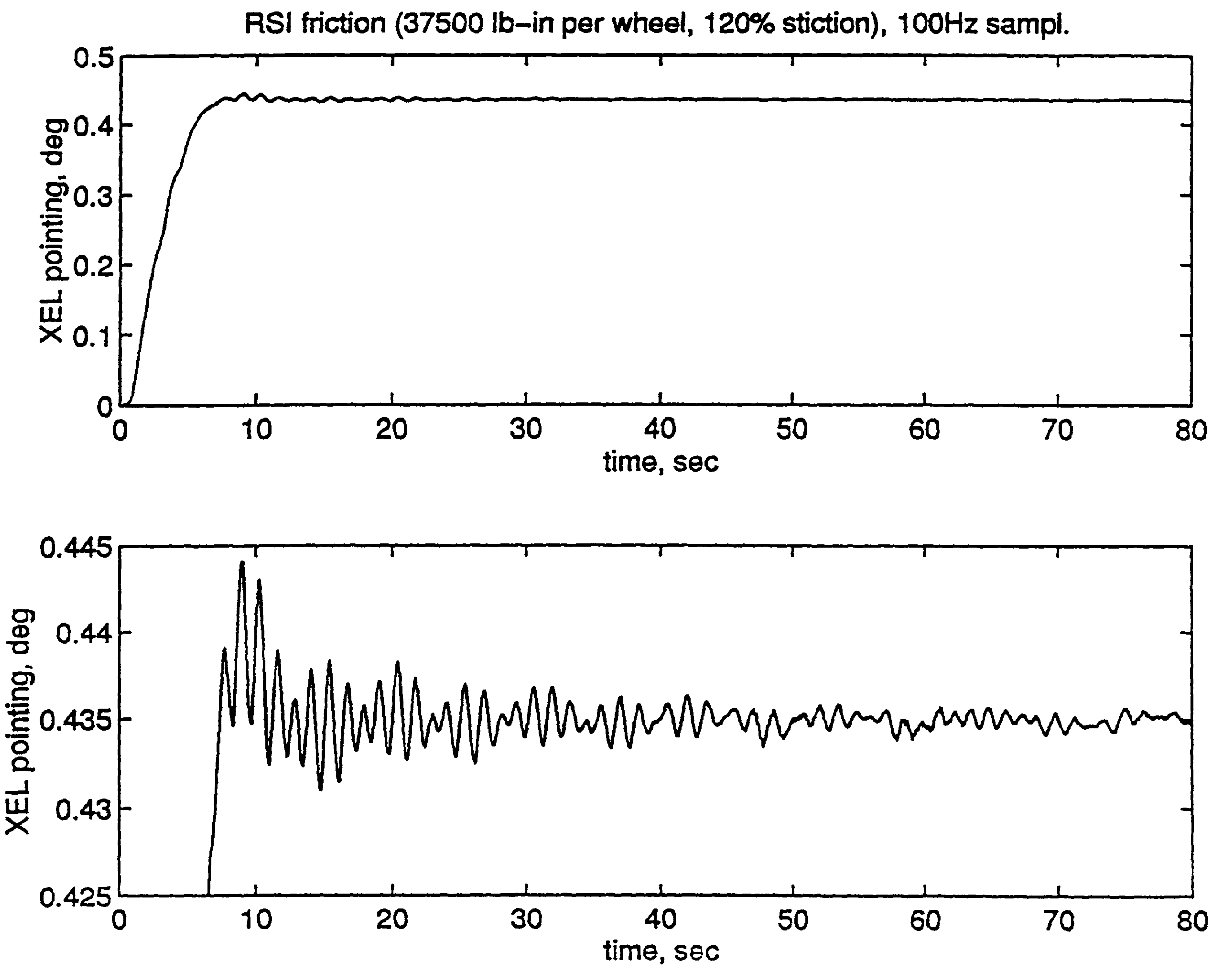

Fig.41. The cross-elevation beam position for 1 deg step command in azimuth, with the preprocessor (a) full figure, (b) zoomed figure.

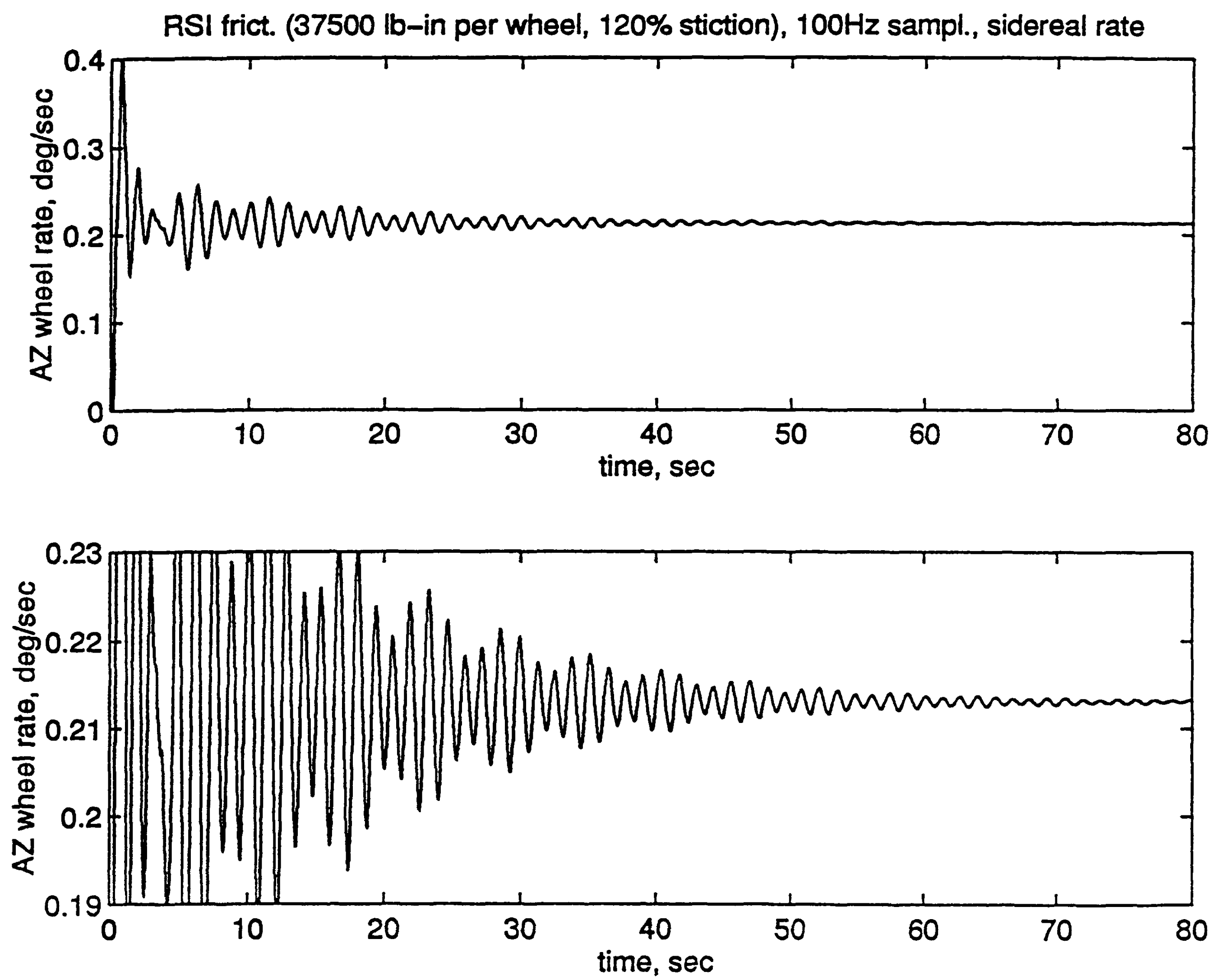

Fig.42. **Wheel rate while tracking at sidereal rate in azimuth, with friction and stiction (a) full figure, (b) zoomed figure.**

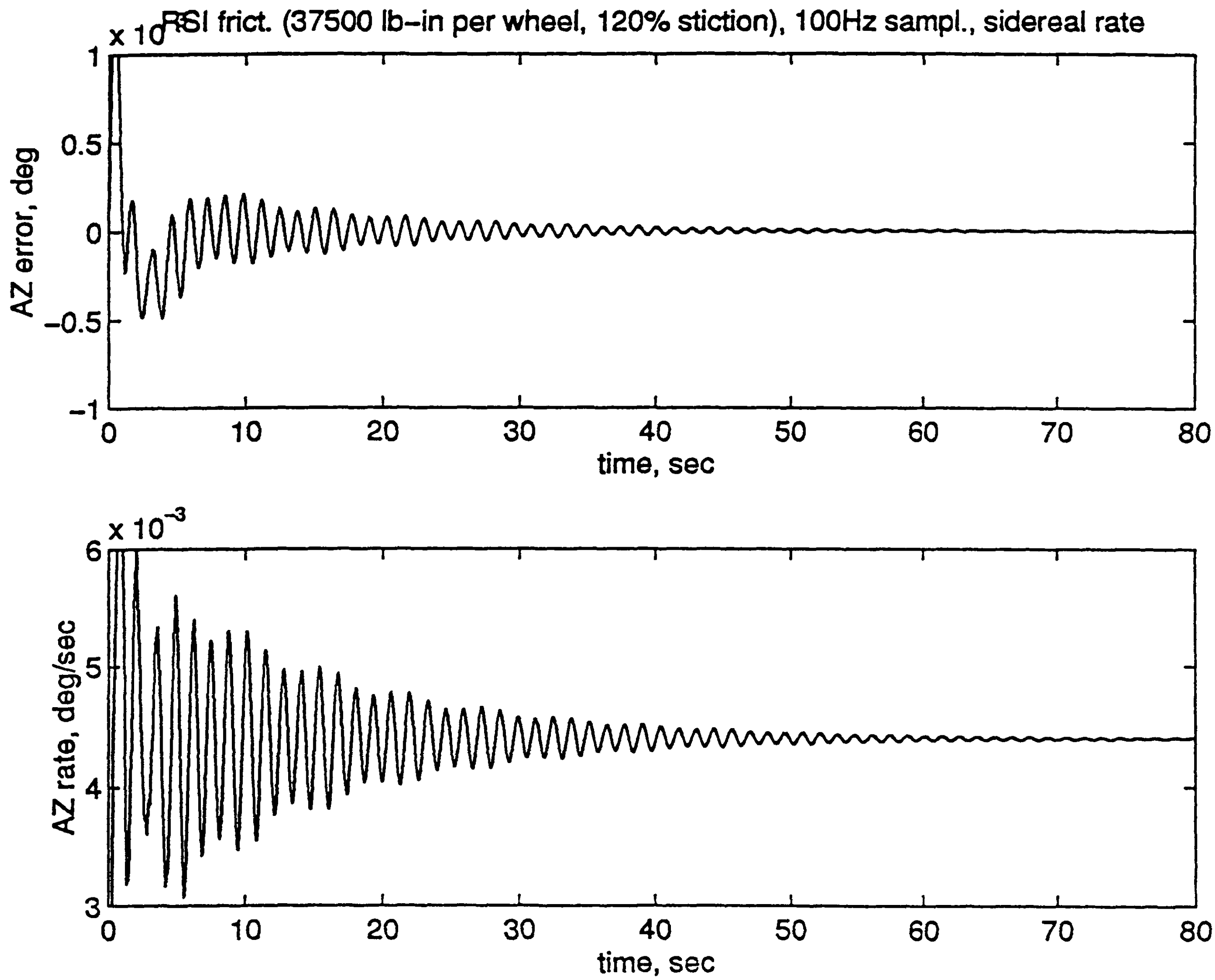

Fig.43. Tracking at sidereal rate in azimuth, with friction and stiction: (a) azimuth encoder error, and (b) azimuth rate.

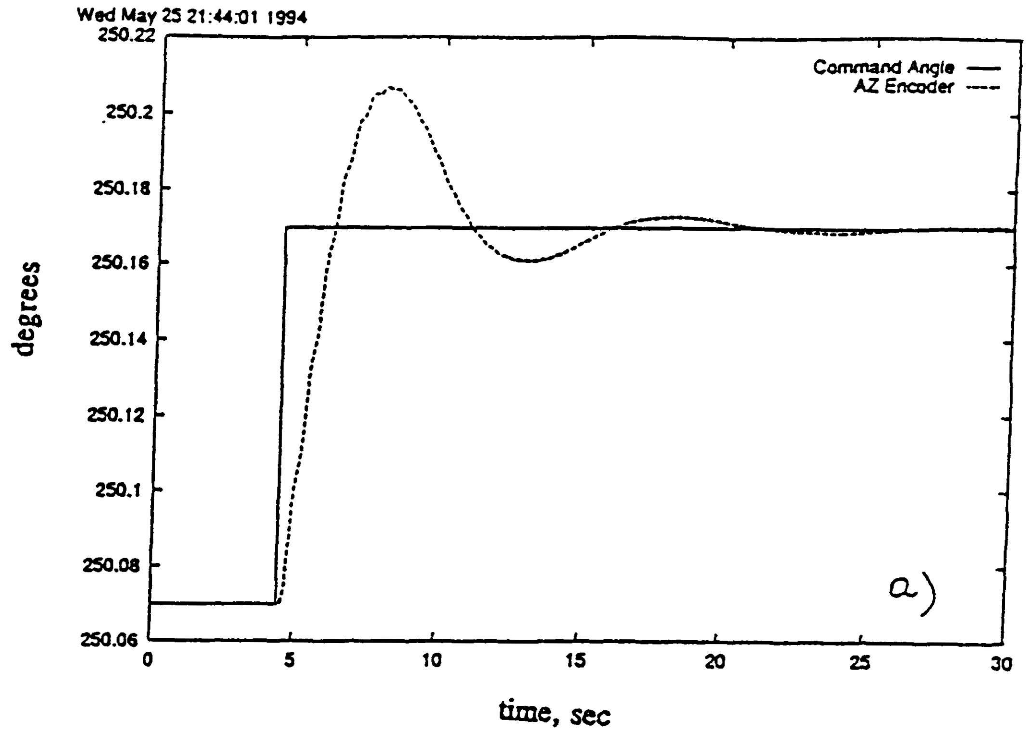

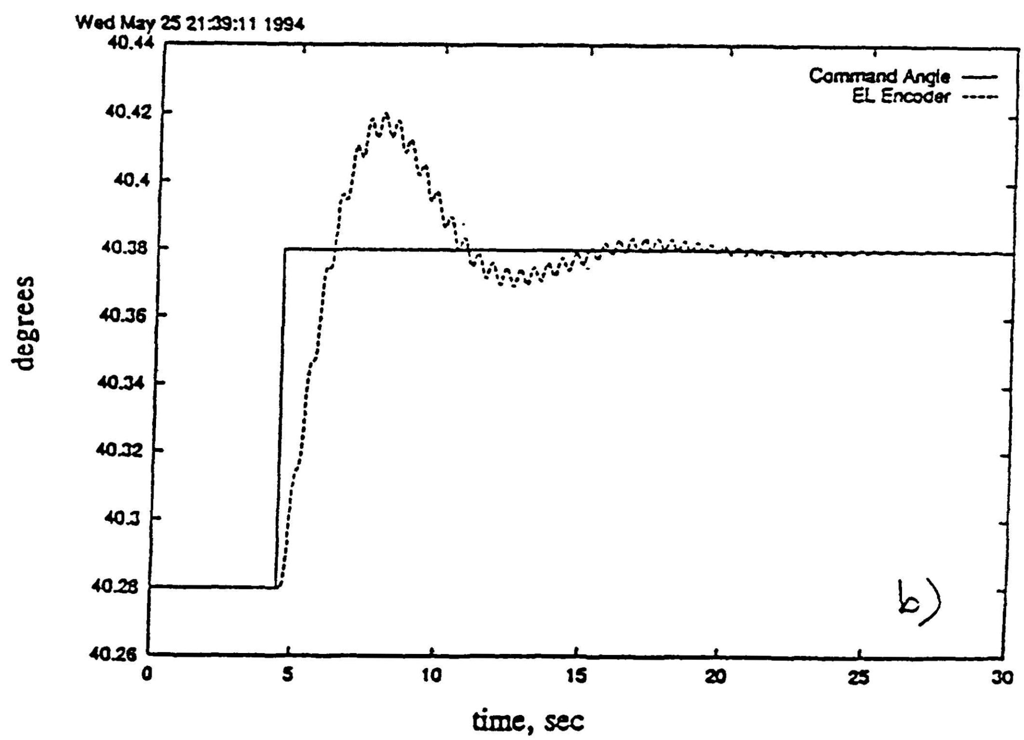

MEASUREMENTS FROM DSN ANTENNAS

Fig.44. Test results with the 10 mdeg step input commands for the DSS-24 antenna (a) azimuth encoder, (b) elevation encoder.

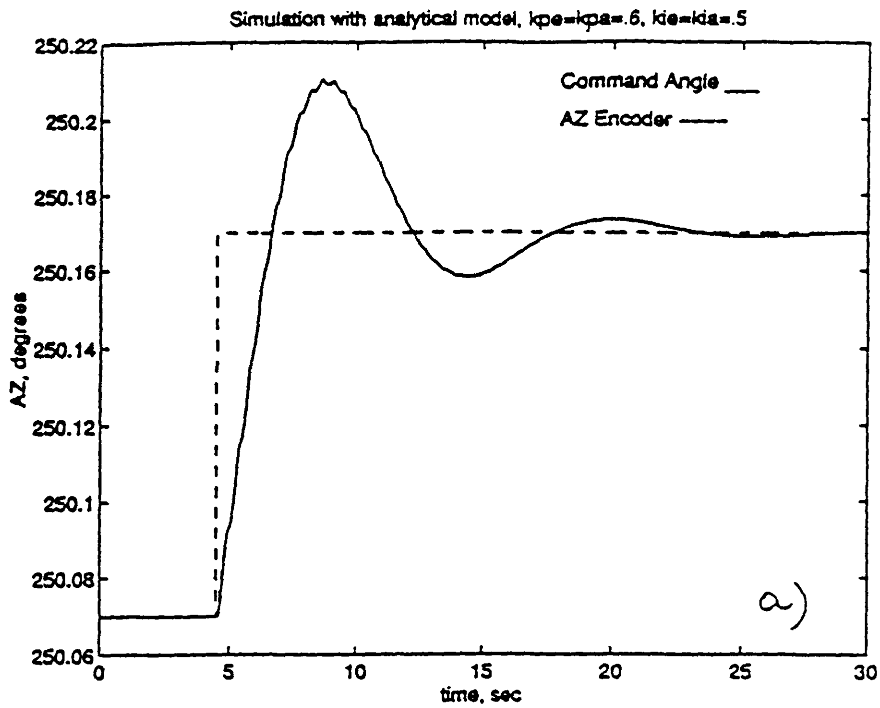

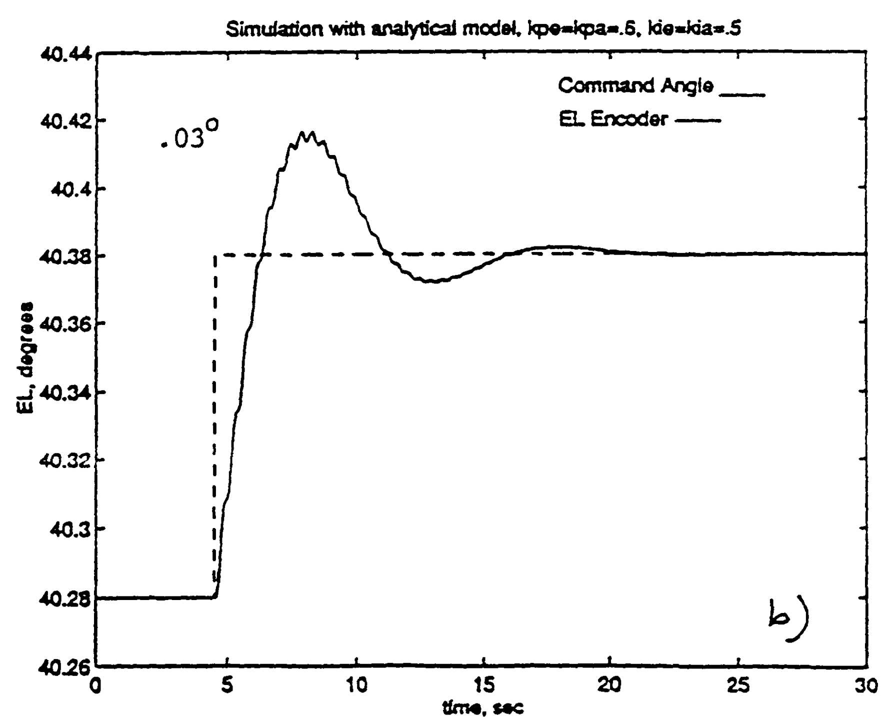

Fig.45. Simulated test results with the 10 mdeg step input commands for the DSS-24 antenna (a) azimuth encoder, (b) elevation encoder.

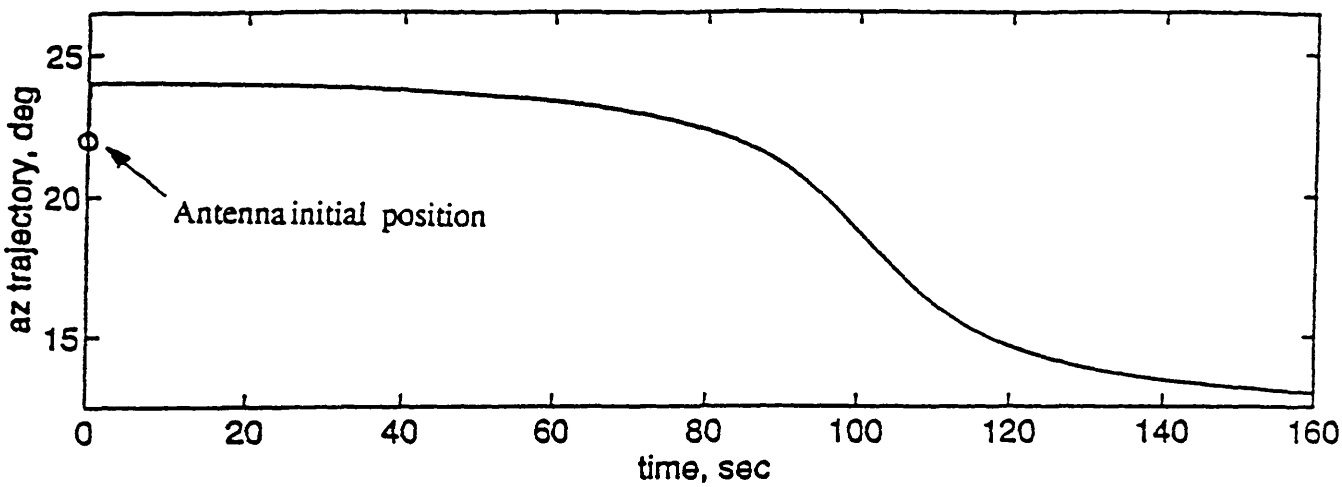

Fig.46. The azimuth trajectory.

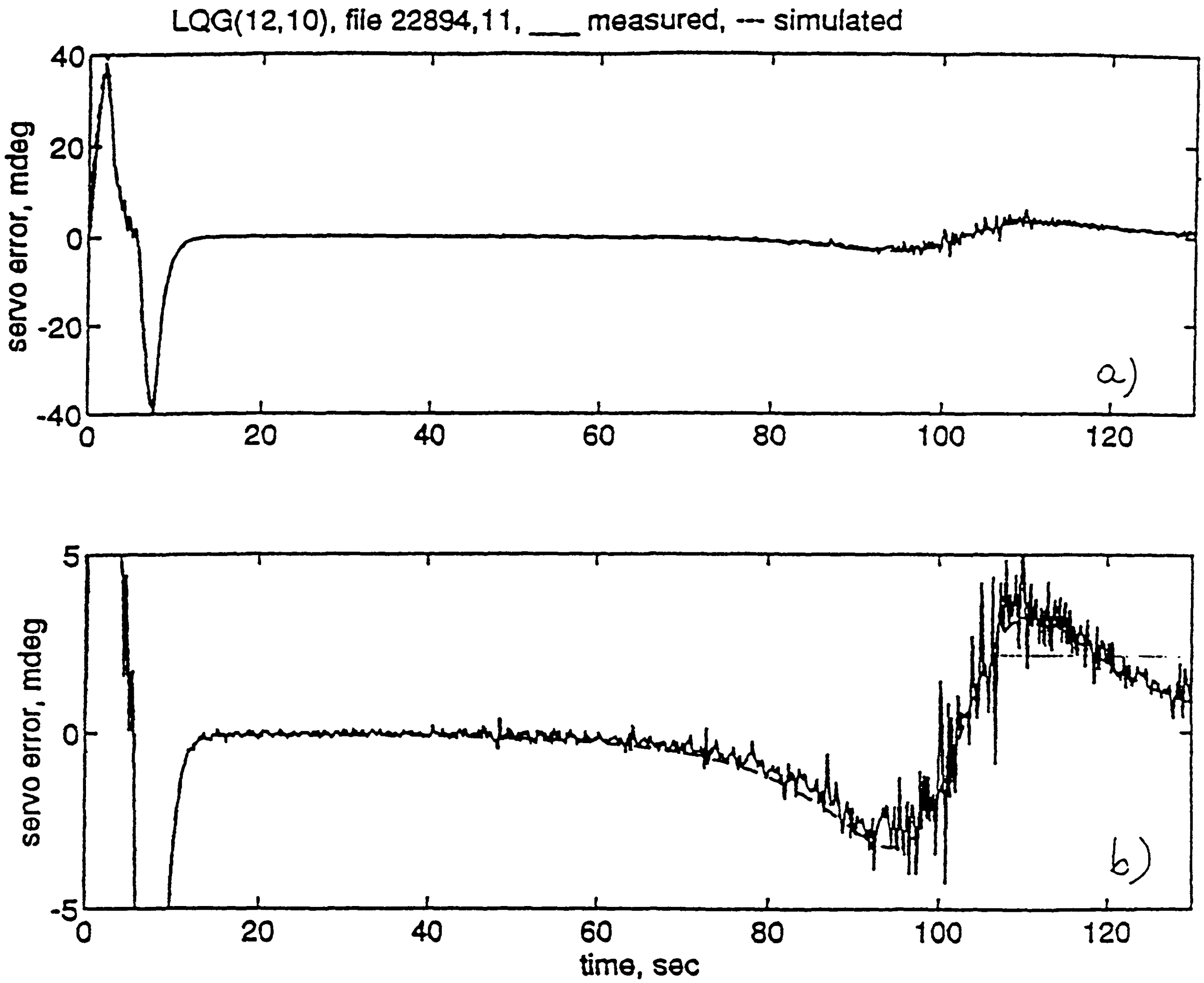

Fig.47. The servo errors, simulated (dashed line) and measured (solid line),
(a) full figure, (b) zoomed figure.